Distribution of thermochemical output and associated ecosystems at the Loki's Castle hydrothermal field

Rasmus Rikter-Svendsen

Master of Science thesis

Department of Earth science

University of Bergen

December 2020

Abstract

Loki's Castle is a hydrothermal vent field situated on the ultra-slow Arctic mid-Ocean ridges, at the boundary of the Mohns- and Knipovich segments (73°30'N, 08°E), and consists of two sulfide mounds and associated black smoker chimneys with extensive diffusive fluid emission in the surrounding area. Though the site has been the target of extensive research since its discovery in 2008, constraints on the quantity and distribution of thermal output from the vent field are poor. In this study a photomosaic made from 3500 images captured of the seafloor in 2018, is used to identify the distribution and types of hydrothermal venting at the site. The orthomosaic generated from the seafloor images provides a full-resolution map of the vent field, allowing highly detailed digitization of biomarkers and hydrothermal deposits associated with hydrothermal outflow across the site. In-situ temperature measurements were integrated to place constraints on the total heat output and its partition between diffuse and focused outflow. Compared to previous estimates of the total heat flux, the results presented here are highly conservative, with a total thermal output of 146-403 MW. $\sim$90% of the thermal output is through diffuse outflow, indicating a substantial amount of subsurface seawater mixing with the high-temperature ($\sim$300°C) fluids. From the heat flux estimates the mass-, volumetric- and chemical fluxes were derived and constrained, providing quantitative data on the major elements emitted through the vent field. Results presented here show that seafloor image surveys, and subsequent photomosaic-generation when coupled with integrated fluid flow measurements (e.g. temperature), is a powerful method to provide robust constraints on the hydrothermal fluxes, and its implications on the overall heat loss on the ridge.

Acknowledgments

First and foremost, I would like to thank my supervisor Thibaut Barreyre for your incredible guidance. Without your intense devotion to science, this thesis would never have come together. Always welcoming any questions, no matter how mundane or complex, with open arms. Your way of thinking is extraordinary, and has changed my entire approach to science.

I would also like to thank all the great people at the K.G. Jebsen centre for deep sea research for being who you are. Participating in the summer cruise of 2019 was an amazing experience, one for which I am immensely grateful.

A special thanks goes out to Francesca Vulcano and Petra Hribovšek for helping me locate and digitize all temperature measurements at Loki's castle. Without your contributions the results would have been substantially poorer.

To all my friends and family, I would like to thank you for all the good times and support over the last five years, resulting in the time of my life

Lastly I would give a special thanks to the students located in the study room "Black Smoker" for providing an extraordinary social environment.

Contents

1 Introduction

A significant part of heat transfer between the deep Earth and the overlying oceans are exchanged through Mid-Ocean Ridges (MOR), making this process a key component in understanding the interaction between the deep Earth and its surface. Comparisons between thermal flow models and measured conductive cooling of the oceanic crust (fig. 1 left) show a significant discrepancy, particularly near- and on-axis (C. A. Stein and Stein, 1994). This discrepancy is attributed to hydrothermal circulation through oceanic crust accounting for a significant amount of lithospheric cooling, particularly near the axis of seafloor spreading ridges and in young oceanic lithosphere (<30Ma) (C. A. Stein and Stein, 1994). Advective flow is more effective at heat removal than conductive cooling, indicating a more focused thermal output in young oceanic crust compared to the conductive cooling taking place through the entire oceanic lithosphere. The total heat loss through cooling of the oceanic lithosphere is estimated to be ∼32 TW, of which 34% (∼11TW) is attributed to hydrothermalism (C. A. Stein and Stein, 1994). Hydrothermal activity at the ridge is closely related to active tectonic and geological processes, such as volcanism, pluton emplacement and serpentinization of deep lithospheric rock. As seawater percolates through the permeable crust it is geothermally heated causing the buoyant hydrothermal fluids to emit trough the crust, often resulting in hydrothermal structures such as black smokers.
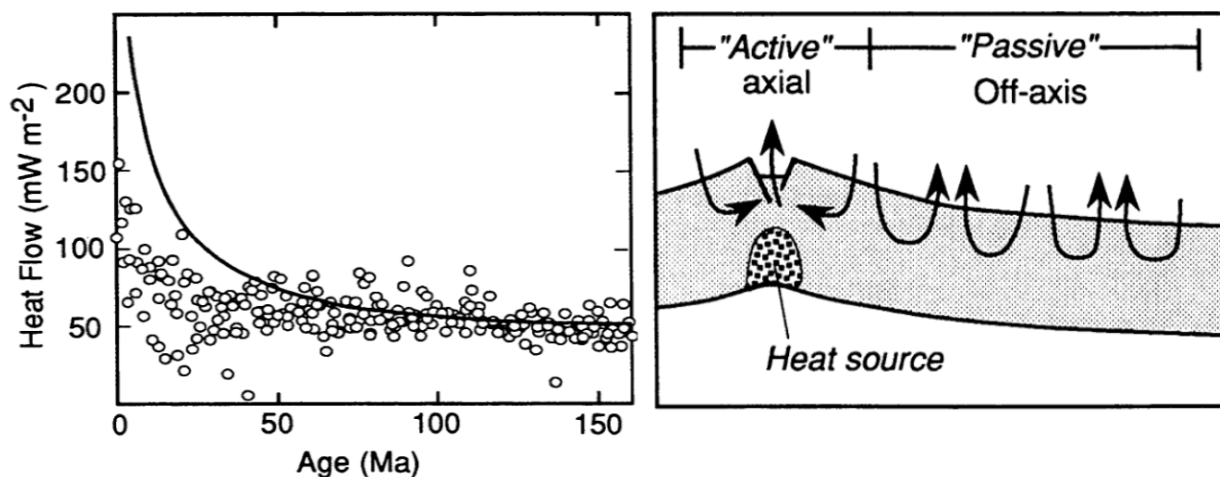
Figure 1: Left: The solid line is expected heat loss based on thermal flow models of the oceanic crust, while circles are measured values of conductive cooling. The discrepancy is most evident in young crustal ages 0-50Ma. From Alt (1995), originally from C. A. Stein and Stein (1994). Right: Model of convective regime in the oceanic crust. High-temperature advection on-axis is driven by a physical or chemical heat source, while off-axis hydrothermalism is driven by passive cooling of young (<30Ma) lithosphere. From Alt (1995).

1.1 Two convection regimes in young oceanic crust

Two kinds of distinct convective, hydrothermal circulation regimes of the oceanic lithosphere were proposed by Lister (1982): active/on-axis and passive/off-axis (fig. 1 right). Active convective systems are located on the axial crest, where energy is transferred from a physical heat source (e.g. a magmatic lens) or an exothermic chemical reaction (e.g. serpentinization) to the fluids. Due to this heat source in close proximity, temperatures are high (T > 300 °C), and fluid circulation is fast and turbulent. Passive systems are situated off-axis, where the heat source driving the hydrothermal circulation exists in the form of conductive cooling of the oceanic crust, resulting in low-temperature (< 50 °C) outflow of hydrothermal fluids (fig. 1 right). 30% of hydrothermal heat flux occurs on-axis or in oceanic crust younger than 1Ma, accounting for 10% of the total heat loss from the solid Earth (~43TW) (Elderfield and Schultz, 1996; C. A. Stein and Stein, 1994). The bulk heat flux through hydrothermal circulation is therefore emitted under passive regimes, while still situated in young (<30Ma) oceanic lithosphere. Old (>30Ma) oceanic lithosphere is highly mineralized (decreased porosity and permeability), and overlaid by a thick sedimentary layer and lack shallow heat sources, thus producing no hydrothermal circulation (Van Dover, 2000).

The hydrothermal circulation system can be separated into three distinct zones: the recharge area, the reaction zone and the discharge zone (Alt, 1995). The recharge area is where the ambient seawater percolates through the oceanic crust, the reaction zone is where the fluids are heated by conduction or emplaced magmatic lense/exothermic reaction and chemically altered. The discharge zone is the area where the buoyant hydrothermal fluids emit through the oceanic crust. Discharged hydrothermal fluids range from slightly above ambient seawater temperatures to ~350°C, depending on the heat mined from the thermal source, and the rate of mixing between high-temperature hydrothermal fluids and cool seawater in the shallow crust. In active hydrothermal regimes the upflow zone is more focused than the recharge zone, whereas passive regimes are characterized by a dispersed outflow zone (Alt, 1995).

1.2 Heat flow and hydrothermal activity along mid-ocean ridges

Since the discovery of hydrothermalism in the 70's in the Galapagos rift (Corliss et al., 1979), hydrothermal circulation were long believed to only exist in fast- and intermediary spreading ridges due to the shallowly emplaced magmatic lens. Later discoveries of hydrothermal vent fields in slow- and ultra-slow spreading ridges, in addition to other tectonic settings such

as back-arc spreading centres and intra-plate volcanic settings, prove hydrothermal circulation to be prevalent in these sites as well (Barreyre, 2013 and sources within). Although sites of hydrothermal venting have been discovered and extensively studied in all aforementioned tectonic settings, the characterization of hydrothermal circulation and subseafloor organization of hydrothermal cells is poorly understood. Thus the causes of difference in hydrothermal circulation at different tectonic settings, melt supplies on-axis, thermal structures of the ridges and characteristics of heat sources are poorly constrained (Wilcock and Delaney, 1996).

Through extensive seismic profiling, it is well documented that fast- and intermediate spreading ridges producing hydrothermal venting typically overlay a well developed melt lens situated at a subsurface depth of 1-4 km (Baker, 2007 and sources within). In contrast to the highly developed melting lenses characterizing fast- and intermediary spreading ridges, even small melting bodies are rarely present underneath slow and ultra-slow spreading ridges, and detected earthquakes are normally deep-seated, indicating that hydrothermal circulation in these localities may penetrate the entire oceanic crust (Baker, 2007 and sources within). The available heat for hydrothermalism can therefore be calculated from the latent and specific heat of cooling basalt and gabbro, although the depth and efficiency of hydrothermal cooling, in addition to crustal thickness and composition, make such estimates highly uncertain (Baker, 2007). Due to the low spreading rate and reduced magmatic feed, intermediate, slow and ultra-slow spreading ridges also allow tectonic extension resulting in exposed mantle material, making ultramafically hosted hydrothermal fields possible along these ridges (Cannat, 1993).

1.3   Hydrothermal flux components

As described by Lister (1982) there are two distinct hydrothermal circulation regimes at different distances to the axis (active on-axis and passive off-axis), although conductive cooling of the oceanic lithosphere still takes place in an advectively dominated area. Therefore the total heat flux of a hydrothermal field can be expressed as the sum of the advective heat flux (Q_a) and the conductive heat flux (Q_c).

As advective cooling is more effective than conductive cooling, the advective heat flux (Q_a) is the dominant component in active hydrothermal regimes and is manifested as hydrother-

mal depositional structures (e.g. chimneys, mounds) and biomarkers (e.g. bacterial mats, tube worms) associated with the outflow. Two types of advective hydrothermal venting have been described: focused, high-temperature venting through chimneys (Q_{af}), which have a measured temperature of $>100°C$ (often 300-400 °C), and diffuse, low-temperature venting through the seafloor which have a measured temperature of $<100°C$, resulting from mixing of cool seawater and hydrothermal fluids (Barreyre et al., 2014; Corliss et al., 1979). The second component of hydrothermal heat transfer is the conductive flux (Q_c), which will vary depending on the distance to the heat source.

1.4 Aim of study

Since the discovery of the Loki's Castle hydrothermal field in 2008 (Pedersen, Rapp, et al., 2010), the area has been extensively studied, though no detailed constraints on the distributions of hydrothermal flux of the area have been placed. Here, a method coupling photo-mosaic imagery to constrain the characteristics and distribution of hydrothermal outflow is presented. By integrating in-situ temperature measurements, the amplitude and distribution of the heat flux components are calculated, from which the mass- and volumetric flow of the vent field are extrapolated. Through integration of previously published chemical data (e.g. Baumberger et al., 2016), the chemical flux of the vent field is also estimated. Heat- and chemical extraction from the Earth's interior through hydrothermal circulation may have significant economical implications for the future, for which good constraints on the fluxes are crucial to quantify the potential.

2 Geological background

2.1 AMOR

The Arctic Mid-Ocean Ridge system (AMOR) is a series of ridges located above the arctic circle (66°), extending from the northern shelf of Iceland, through the Norwegian sea and ends at the siberian shelf in the Laptev sea (Pedersen, Thorseth, et al., 2010). The ridge system consists of six segments (the Kolbeinsey ridge, the Mohns ridge, the Knipovich ridge, the Molloy ridge, the Lena through and the Gakkel ridge) and is alongside the Southwest Indian Ridge the only discovered ridge system that represents ultraslow spreading (<20 mm

a^{-1}) (Pedersen, Thorseth, et al., 2010). Hydrothermal activity along ultra-slow spreading ridges is more common than previously believed, with approximately 20 sites of active or extinct hydrothermalism discovered along the AMOR, with current active searching for more sites (Pedersen, Thorseth, et al., 2010). The study area of this thesis is the Loki's Castle hydrothermal field (LCHF), discovered in 2008 (fig. 2).
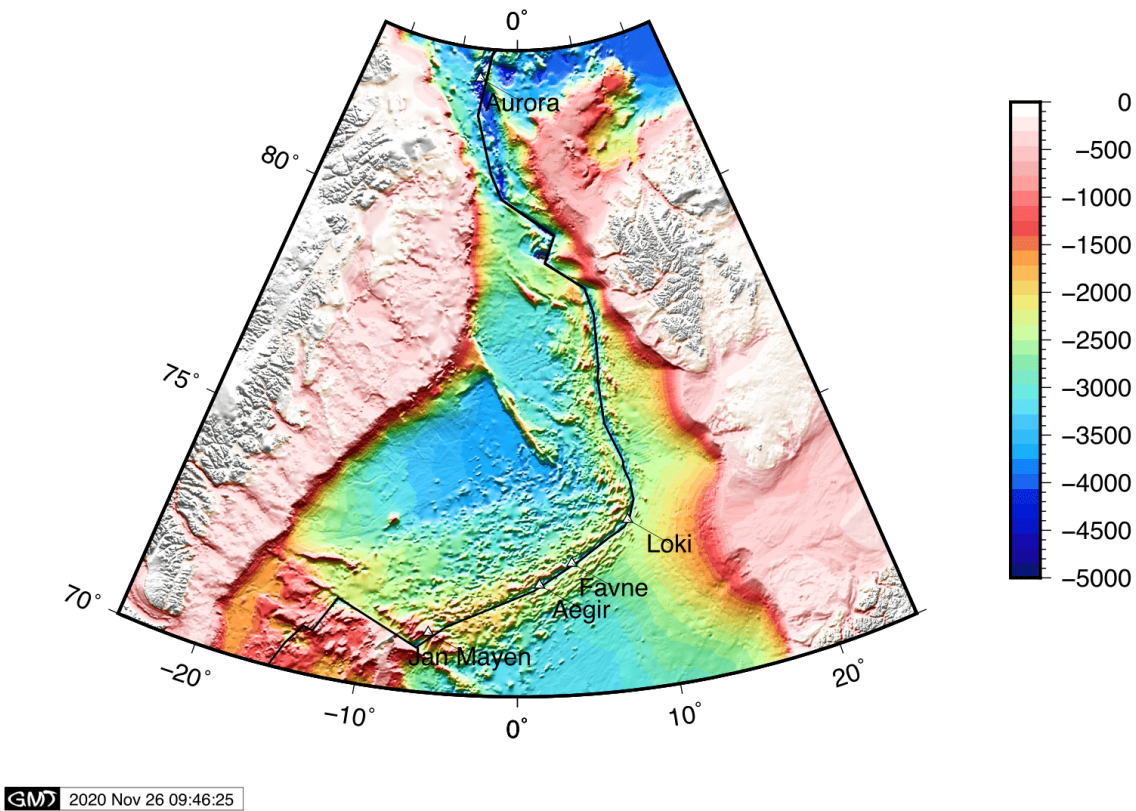
Figure 2: Map showing the Arctic mid-Ocean Ridges, and the location of the Loki's Castle Vent Field at the transition between the Mohns ridge and Knipovich ridge. Courtesty of T. Barreyre.

2.2 Loki's Castle

Mohns ridge is an obliquely spreading ridge with a spreading rate estimated as ∼15.6 mm*yr^{-1} for the last 10 Ma (Mosar et al., 2002, Vogt, 1986). The LCHF is located at 73°30'N 08°E, where the Mohns ridge transitions into the Knipovich ridge (Eickmann et al., 2014). The vent field situated at a depth of ∼2300m, on the crest of an axial volcanic rift (fig. 3). The vent site itself consists of four distinct areas: two mounds of hydrothermally associated sulfide deposits (eastern and western mound), each with actively venting black

smoker chimneys situated on top, and two areas of purely advective diffuse outflow and associated biomarkers and hydrothermal deposits (barite field and oasis).
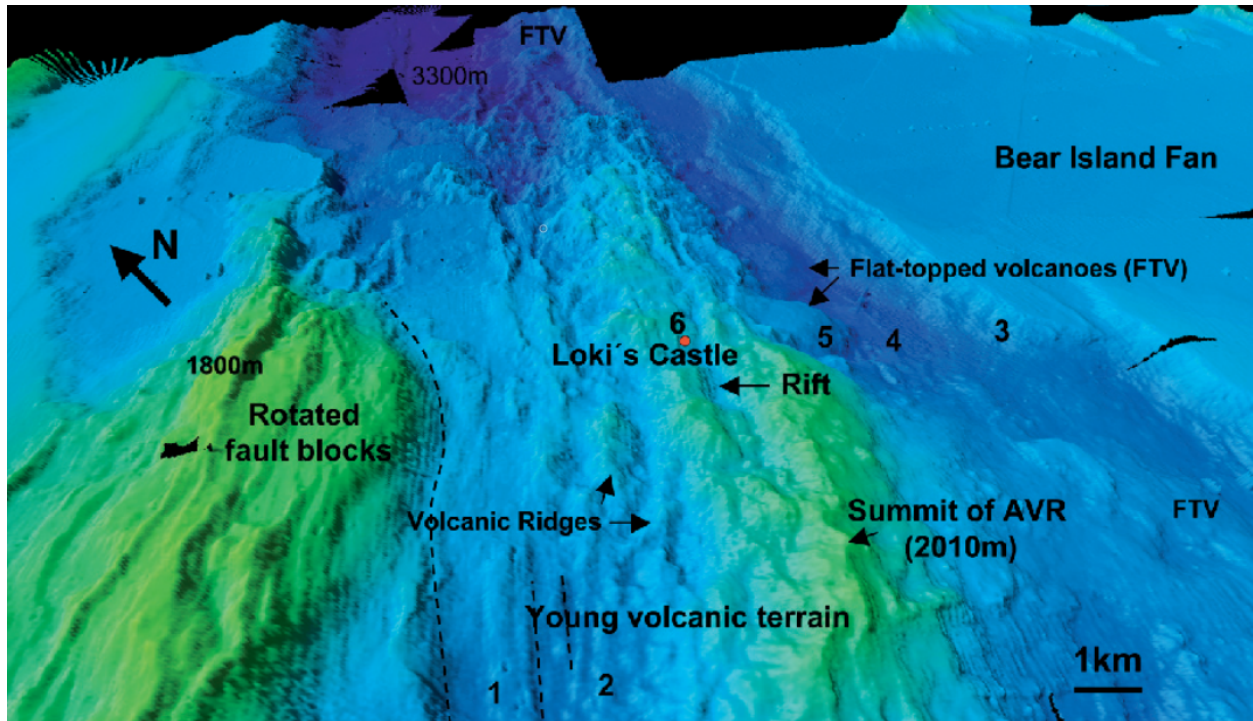
Figure 3: The location of Loki's Castle on the axial volcanic rift in addition to surrounding seafloor terrains. From Pedersen, Thorseth, et al. (2010)

2.2.1   Western mound (Sleepy, Menorah & Camel)

The western mound (73°34.01'N, 08°09.39'E) is 20-30m tall, and has a diameter of 150-200m. The mound itself consists primarily of hydrothermally assosciated sulfides (pyrite, sphalerite and pyrrhotite) (Pedersen, Rapp, et al., 2010). Situated on top of the mound there are three high-temperature (>300°C) black smoker vents evenly distributed from the northwest to the southeast, with a spacing of ∼3-5m. The vent localized in the northwest is named *Sleepy* as it shows the least visible activity of the three smokers. The vent located in the middle is named *Menorah*, and the southeastern vent is named *Camel* (Fig. 4). *Menorah* and *Camel* consists of several branching chimneys, while *Sleepy* consists of one bulbously shaped chimney.

Figure 4: Modified ROV footage showing the three black smoker vents on the western mound, with a heading of ∼50°. Vent A is Menorah, B is Camel and C is Sleepy. The white, mottled patches surrounding the chimneys consist of microorganisms living of the chemical disequilibrium between the outflowing hydrothermal fluids and surrounding seawater.
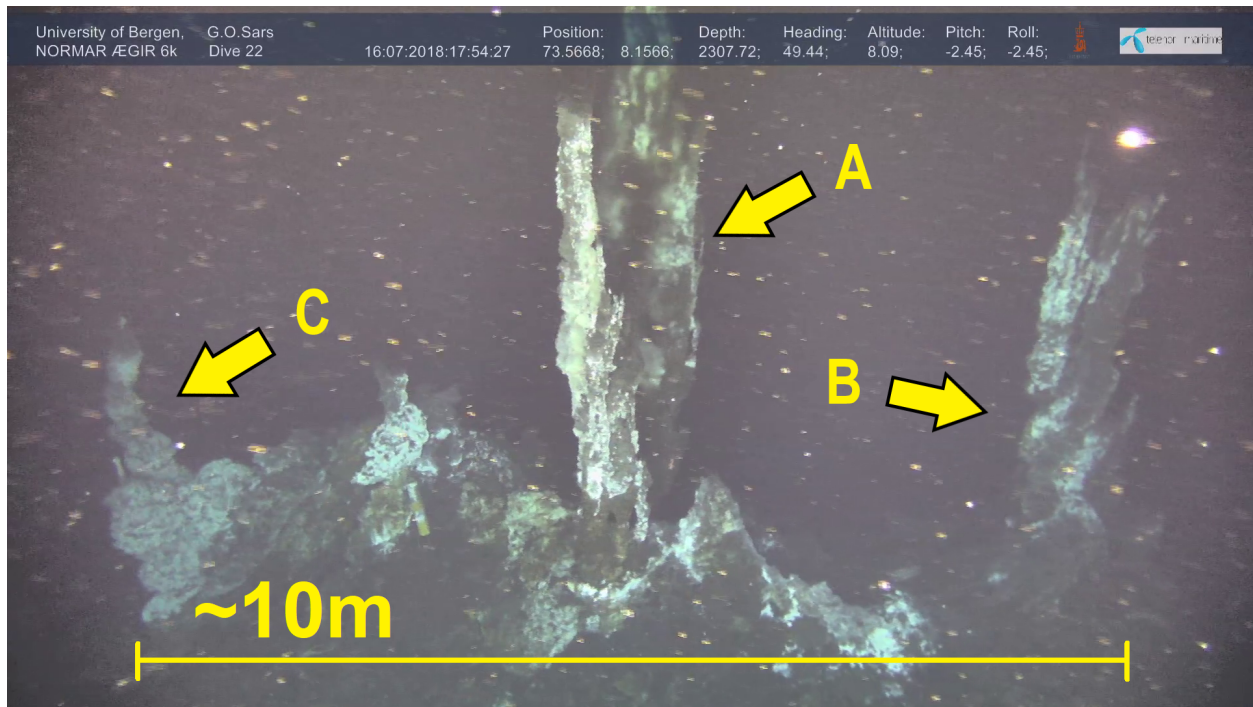
2.2.2 Eastern mound (Jõao)

The eastern mound is situated approxiately 150m to the east of the western mound (73°34.01'N, 08°09.39'E), and has the same dimensions and composition as the western mound. However, where the western mound hosts three hydrothermal vents, the eastern mound only host one vent at the top named Jõao. Although the most striking visual feature of the mound is the high-temperature, focused vent (Jõao), large areas of the mound is covered by bacterial mats, indicating a high fraction of diffuse outflow.

2.2.3 Barite field

In the eastern area of LCHF a large (∼250m^2) area of low-temperature (∼20°C), hydrothermal outflow named the barite field is situated (Pedersen, Rapp, et al., 2010). The name originates from the numerous small (<1m) barite chimneys present in the area and associated microbial mats (fig. 5). The barite field also hosts a rich vent fauna including, but not limited to, microbial mats, colonies of tube worms, vent fish, amphipods, and sea urchins.
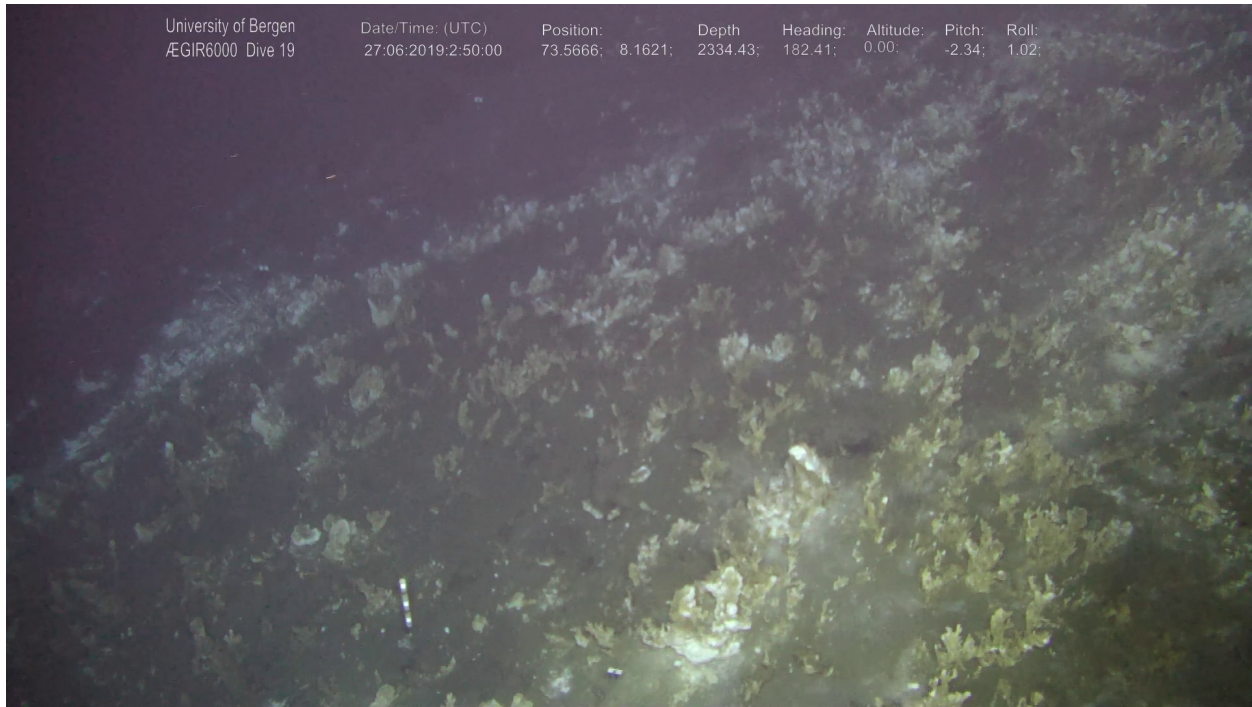
Figure 5: ROV footage (captured in 2018) from the barite field, showing the extensive distribution of hydrothermally associated deposits and biomarkers.

2.2.4 Oasis

Approximately 40m north of the barite field (the north-eastern area of LCHF) a ∼20x20m area, hosting large (∼5m) colonies of tube worm and bacterial mats associated with diffuse hydrothermal venting, is situated. This area is named the oasis, and running through it is a ∼4m tall outcrop with a strike angle of ∼40°C, consisting of pillow basalt. From the cracks in the outcrop, shimmering low-temperature (∼20°C) hydrothermal fluids are emitted, with associated biomarkers and hydrothermal deposits.
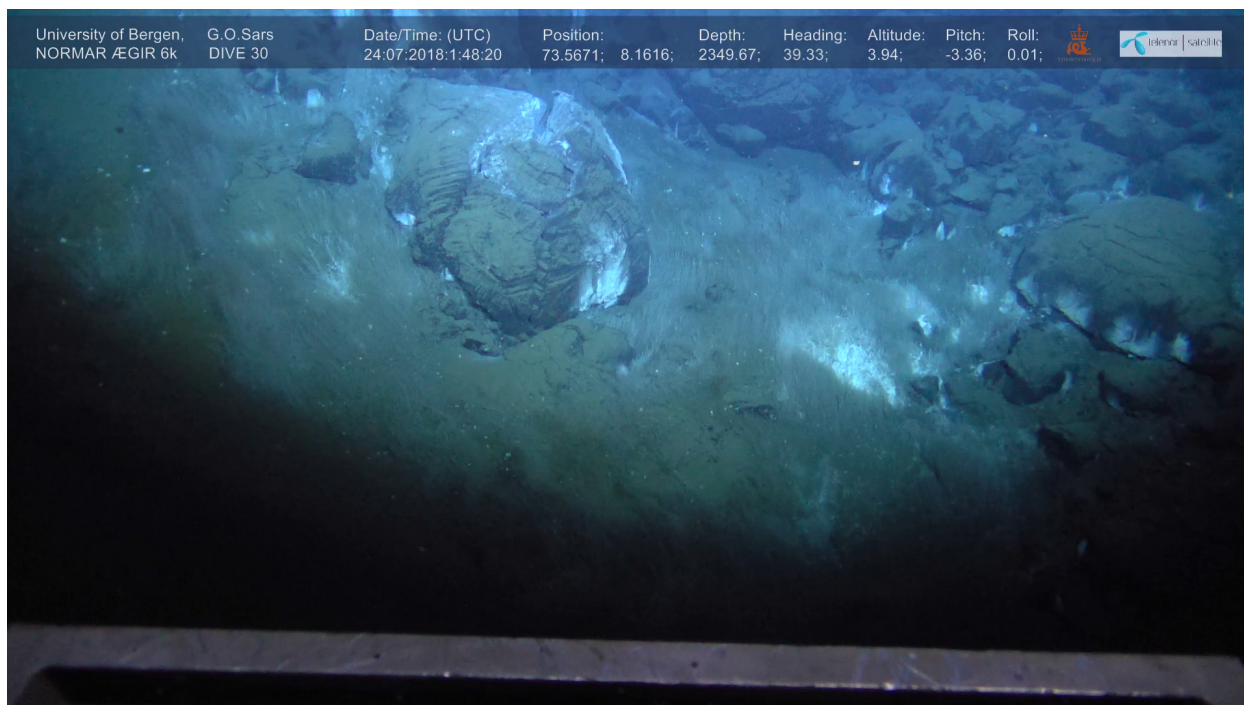
Figure 6: ROV footage (captured in 2018) from the Oasis, showing hosted tube worm colonies and white micro-bacterial mats, in adittion to emplaced basaltic pillows.

3 Materials and methods

3.1 Data collection

All data used in this thesis were collected during cruises to the AMOR carried out by the K.G. Jebsen centre for Deep Sea Research aboard R/V G.O. Sars. The research cruises took place in the summer of 2017, 2018, 2019 and 2020, and were aptly named CDeepSea17,-18, -19 and -20. One of the goals of these research cruises is to locate, map, monitor and sample hydrothermal vent fields on the AMOR.

3.1.1 ROV data

3.1.1.1 Seafloor image survey

Seafloor image surveys were conducted in the CDeepSea18 cruise to create a high resolution photomosaic of the Loki's Castle hydrothermal area. To conduct these surveys, the remotely operated vehicle (ROV) Ægir 6000 was utilized. A total of three surveys were conducted: one to cover the eastern mound and barite field (survey #1), one to cover the western mound

and associated vents (survey #2), and one to cover the fault scarp in the oasis (survey #3). A DSC 24,000 digital still camera were mounted vertically on the ROV for survey #1 and #2,while survey #3 were conducted using a modified GoPro 12MP digital still camera mounted horizontally on the ROV.

The survey covering the eastern mound and the barite field (survey #1) were conducted during dive GS18_218_ROV30, capturing 2617 images with a frequency of 1/15Hz. The ROV moved at an altitude of 4m above the seafloor during the survey with a horizontal velocity of 0.13m/s, corresponding to a ∼10 hour survey. The survey covering the western mound and associated vents (survey #2) were conducted during dive GS18_218_ROV31, capturing 657 images at a the same frequency as survey #1 (1/15Hz). The ROV speed and altitude were also the same as in survey #1. Survey #2 took lasted ∼2 hours 30 minutes. Survey #3, covering the fault scarp, were also conducted during dive GS18_218_ROV31. The survey captured 263 images at a frequency of 1/5Hz, and lasted ∼20 minutes. The ROV altitude and velocity was not constant as this survey did not cover a horizontal plane. A total of 3500 high-quality photos were acquired during the three surveys for further processing, although only the photomosaics resulting from survey #1 and #2 were used in this thesis.

The process to create a photomosaic from raw images will be briefly explained here, although the full description is available elsewhere (Prados et al., 2011, Campos and Quintana, 2019). The images are first pre-processed to correct for uneven illumination, equalize the intensity of the images and correct the geometrical distortion from the camera lenses (Barreyre et al., 2012). Pre-processed images are then scaled, rotated and projected using vehicle navigation to create a high resolution, georeferenced mosaic which can be used to visualize and extract data (Campos and Quintana, 2019). After the photomosaic has been created, blending and color correction is applied to increase the photomosaic quality and visual accuracy. A total of two photomosaics (ROV_30 & ROV_31) were created, representing respectively Loki East (João, barite field & oasis) and Loki West (Sleepy, Menorah & Camel).
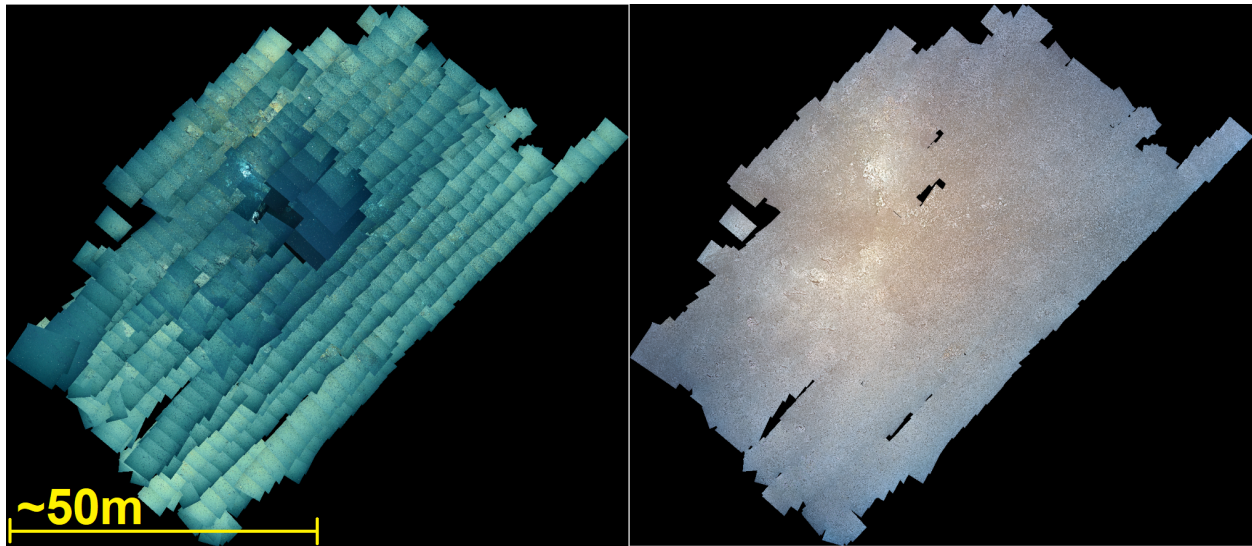
Figure 7: Photomosaic GS18_ROV31 after scaling, rotation and projection. The left box shows the raw, unblended images preserving all details from the raw images. The right box shows the photomosaic box post-blending, creating a smooth, evenly illuminated photomosaic.

3.1.1.2   ROV footage

Ægir 6000 carries two IMENCO Spinner II Shark cameras mounted to the front and top of the ROV, providing video feeds to the ROV pilots and research vessel. Video footage from these two cameras were later used to manually recognize and mark the location of deployed instruments on the generated photomosaic.

3.1.2   Temperature

A total of 29 dedicated temperature sensors were deployed between 2017 and 2020, in addition to other instruments containing temperature sensors as a secondary feature, some of which are included in this thesis. Dedicated temperature sensors were deployed for long-term monitoring of hydrothermal outflow, over the period of ∼one year per deployment. Each temperature logger were deployed and recovered using the ROV.

3.1.2.1   Low Temperature logger (loT)

To conduct temperature measurements in areas of diffuse hydrothermal outflow, low-temperature self-recording loggers for hydrothermal vent monitoring (loT), developed and produced by Woods Hole Oceanographic Institution's (WHOI) Multidisciplinary Instrumentation in Support of Oceanography (MISO), were deployed (Fig. 8). Each loT probe contains one digital

11

temperature logger, which can record temperature in the range from 0°-60°C at a 12 bit resolution, in a titanium casing rated to a depth of 3750m (D. Fornari et al., 1998). The battery of the loggers allow for a sampling rate of ~14min over the course of one year.

In total, 16 loT probes were deployed in the Loki's Castle hydrothermal field (four in 2017, six in 2018 and six in 2019), each left in place over the course of ~one year before being retrieved during the next years cruise. The temperature data were then downloaded from the logger before the logger were reset and either redeployed or sent to storage. Due to condensation or seawater entering the electronics housing, the temperature data logged by two of the loT probes deployed in 2017, and one deployed in 2019, were corrupted.

Figure 8: A low-temperature self-recording logger produced by MISO to record the temperature of diffuse, hydrothermal outflow. The temperature sensor is located in tip of the narrow rod, while the broader titanium housing contains the electronic components to keep them away from direct contact with the hydrothermal fluids. From D. J. Fornari (2009).

3.1.2.2 High temperature logger (hiT/hiTT)

High-temperature (~300°C) hydrothermal fluids from focused venting were measured using two different generations of temperature loggers. Both generations are developed and produced by WHOI MISO. The older generation (hiT) consists of a temperature logger housed in a 72 cm titanium rod, which is connected to a titanium housing containing the electronic components. This acts as an extra layer of protection from the high-temperature, corrosive fluids. The temperature range of the hiT probe is 0°C - 450°C at a 12-bit precision, with an operating depth up to 3750m. The battery allows for an operating life of 3 years in deep-sea temperatures ($\sim 2 - 4$°C) (D. Fornari et al., 1998).

The next version of the WHOI MISO high-temperature loggers (hiTT) improves on the previous generation (hiT) with a 22-bit precision replacing the 12-bit precision of the temperature sensor among other features (Perrone, 2009). The depth rating is also improved with a maximum operating depth of 6000m. For all purposes of this thesis, the two generations are interchangeable.

A total of 13 high temperature loggers were deployed at LCHF in the period 2017-2020 (seven in 2017, one in 2018 and five in 2019). In a identical manner to the loT, they were left recording for ~one year before retrieval during the next years research cruise. However, due to the corrosivity and extreme temperatures of the high-temperature fluids and porosity and instability of the hydrothermal chimneys, ~80% of deployed sensors were recovered with exploitable data and ~20% of sensors were damaged or lost.

3.1.2.3 T-sword

Temperature readings of the ocean floor were taken during the GS18 cruise by using a device named the T-sword. This consists of a hiT probe where measuring tape was placed on the titanium rod to visually measure the distance from the temperature sensor to the ocean floor as the sensor were pushed into the sediments by the ROV. At 5-10cm intervals the movement of the probe was stopped to allow for thermal equilibria. Temperature data was then downloaded from the logger after the ROV resurfaced. While the T-sword data does not contain temporal fluctuations in temperature, it does provide a large number of single-value measurements covering a larger area than loT and hiT/hiTT data.

3.1.2.4 IGT

Samples for fluid chemical compositions were collected by the *Hydrothermal Fluids* group of Associate Professor E.P. Reeves using Isobaric gas-tight (IGT) titanium fluid samplers (Seewald et al., 2002, Viflot et al., 2019). These IGTs use compressed gas to keep the fluid sample at seafloor pressure to prevent degassing of the sample (Seewald et al., 2002). Thermocouple temperature sensors are also attached to the IGT samplers, providing real-time temperature readings of the hydrothermal fluids during sampling with an accuracy of $\pm 1°C$. While the chemical composition of hydrothermal fluids is the main object of these samples, the temperature data is used in this thesis to further the number of data points.

3.1.2.5 Incubator

In-situ incubators were deployed at the LCHF in 2017, 2018 and 2019 to cultivate microbial life at the seafloor. The incubators consist of a 60cm long metal cylinder with a temperature sensor running through the length of the rod. The lower half of the incubator contains four chambers for microbial cultivation (for which the incubator was designed), but only the temperature data from the incubators will be included in this thesis. Four temperature sensors are situated in the incubators (one in each inoculation chamber), although to prevent biasing only the temperature sensor closest to the seafloor ($\sim$15-20cm, depending on how far the incubator is pushed into the sediments) is used in this thesis.

3.1.2.6 Temperature gradient board

A temperature gradient board, consisting of a 47cm tall board mounted with seven evenly spaced high-presision low-temperature loggers with a distance of 7cm between each logger (*Cruise Report GS18-218*, 2018), were deployed in the hydrothermal plume right above the black smoker João to measure the vertical temperature gradient of emitted high-temperature fluids (fig. 9). Only one measurement with the gradient board is included in this thesis, from which the calculated flux is multiplied by the number of focused vents at the LCHF.
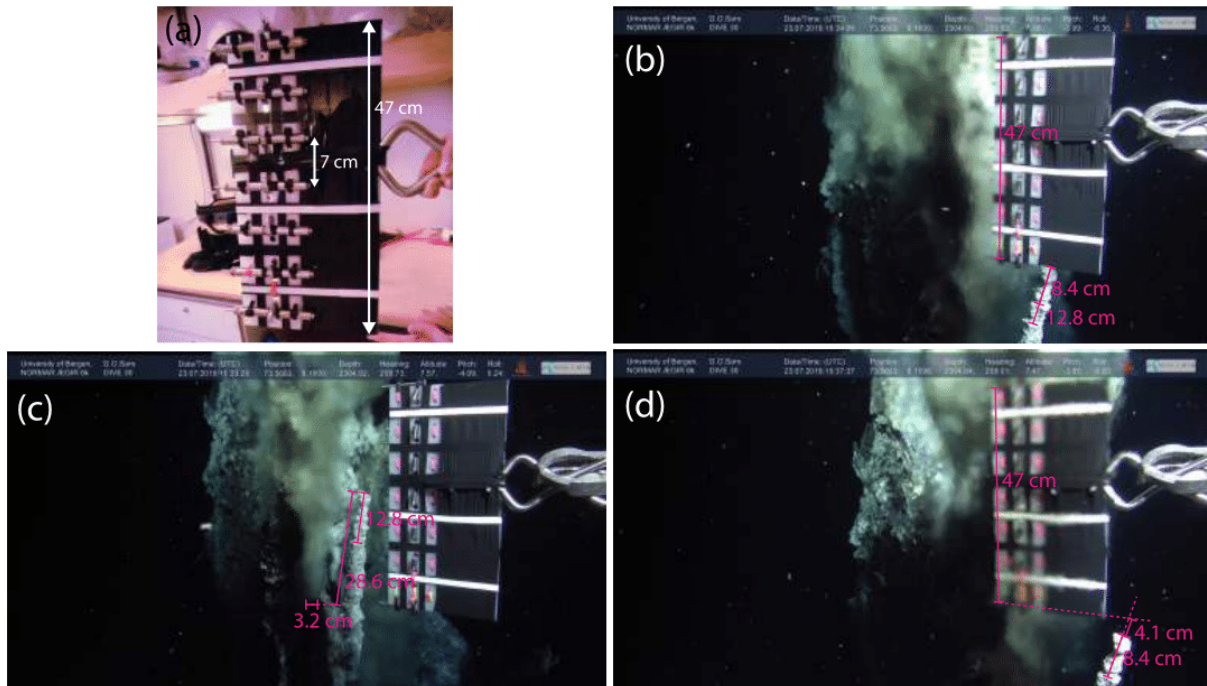
Figure 9: Temperature gradient board in the plume of high-temperature hydrothermal fluids emitted by the black smoker João. The dimensions of the board is known, allowing the dimensions of the black smoker, active orifice and hydrothermal plume (and thus heat flux) to be extrapolated. Courtesy of T. Barreyre.

3.1.2.7 Gravity Core

A ~5m long gravity corer equipped with three temperature sensors were used to measure the vertical temperature gradient in the sediments at the LCHF. The core itself consists of a steel corer lined with a plastic inside and a steel casing holding a copper core catcher to prevent the sampled sediments from escaping the core (*Cruise Report GS18-218*, 2018). Temperature loggers produced by ANTARES Datensysteme GmbH were mounted to the outside of the steel barrel at a distance of 50cm, 200cm and 350cm from the bottom, with a sampling interval of 5 seconds (S.L. Jørgensen, personal communication, December 2, 2020). Temperature data collected with this gravity core will be included in this thesis while the sediment core record is omitted.

3.2   Analytical methods

3.2.1   Mosaicviewer

The two photomosaic boxes can be loaded into a software developed by the Girona Underwater Vision and Robotics, named Mosaicviewer. This software allows for zooming and panning of high-resolution photomosaics in addition to creating/importing/exporting points, lines and polygons as UTM coordinates. One more key feature is the ability to load the raw images used to create a certain area of the photomosaic for more detailed images of the seafloor. Once the photomosaic boxes were created and imported to Mosaicviewer, all visible structures associated to hydrothermal outflow were digitally marked at full resolution either as points, lines or polygons. Digitized structures were therefore categorized by type to gain further insight in the nature of distinct structures and if there is any correlation between temperature, surface area and temperature. All instruments deployed at the LCHF relevant to this thesis were also marked on the photomosaic. Files containing the coordinates of all structures were then exported for further analysis in Matlab (e.g. aquiring the surface area of each distinct structure).

3.2.2   Constraining the heat flux

3.2.2.1   Digitization and integration of in-situ measurements

Since the heat transfer of hydrothermal vent fields consists of two components (advective and conductive), the total heat flux of LCHF is as follows:

$$Q_{tot} = Q_a + Q_c \tag{1}$$

where Q_{tot} is the total heat flux, Q_a is the advective heat flux and Q_c is the conductive heat flux. Since the advective flux is carried by both focused, high-temperature venting and diffuse, low-temperature venting, the total advective heat flux is as follows:

$$Q_a = Q_{af} + Q_{ad} \tag{2}$$

where Q_{af} is the advective focused heat flux, and Q_{ad} is the advective diffuse heat flux. A simple model showing the partitioning of heat flux components, and methods of constraining

them, are presented in figure 10. The photomosaic resulting from the ROV survey is used to constrain the surface area of advective diffuse outflow on a field/mound scale, which by incorporation of temperature measurements, can place constraints on the diffusive heat flux (Q_{ad}). To constrain the advective focused heat flux (Q_{af}), temperature gradient array measurements are used as illustrated in figure 10. Temperature measurements from GC data are incorporated to constrain the conductive heat flux (Q_c), which mainly takes place on a ridge scale.
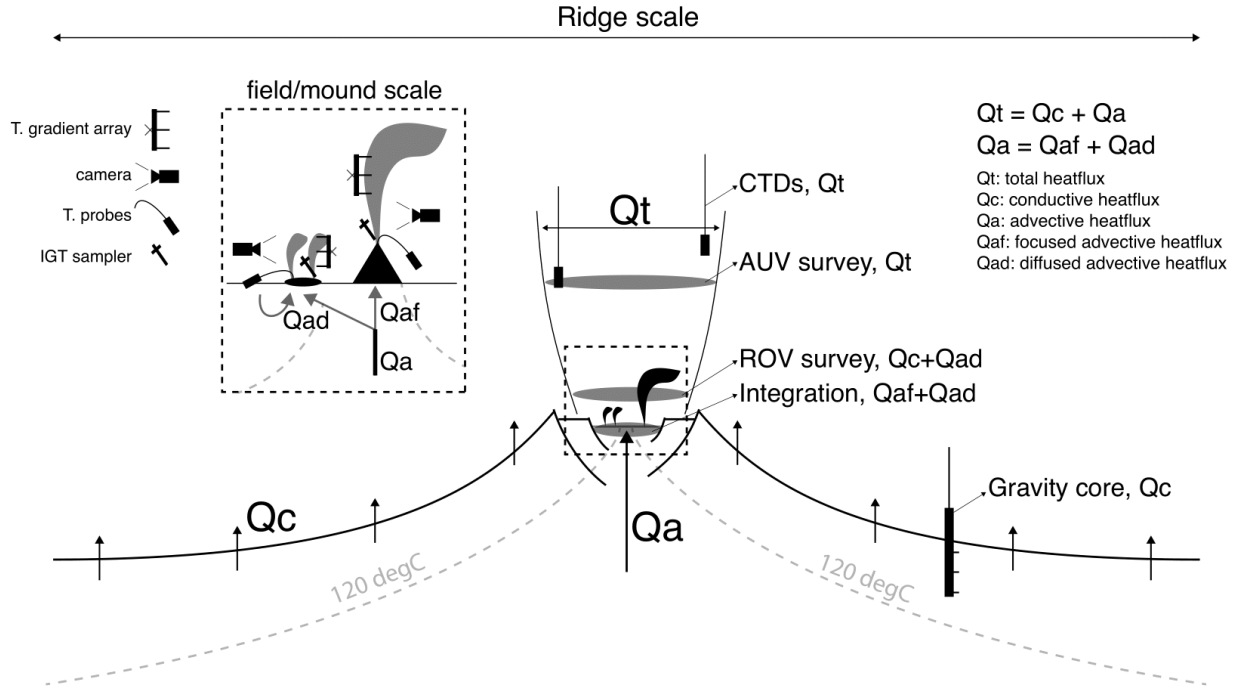
Figure 10: Conceptual model showing the partitioning of all heat flux components and which methods may be used to constrain them. Courtesy of T. Barreyre.

Since focused venting occurs at high temperatures and produces distinct hydrothermal chimneys (black smokers), constraining the advective focused heat flux (Q_{af}) relies on both quantifying the advective heat flux per vent and the number of chimneys and orifices on each mound. The formula for the advective focused heat flux writes:

$$Q_{af} = Q_v * nVents \tag{3}$$

where

$$Q_v = \pi * r^2 C_p \Delta T v \rho \tag{4}$$

17

where Q_v is the heat flux of a vent and $nVents$ is the total number of vents. r is the radius of the vent orifice, and ΔT is the temperature difference between the emitted fluids and ambient seawater. C_p, v and ρ are respectively the heat capacity, velocity and density of the emitted high-temperature fluids. The temperature difference, velocity and orifice radius can be constrained through modeling turbulent plume to fit the temperature gradient board data (described in detail in paragraph 3.2.2.3).

Constraints on low-temperature, diffuse heat fluxes have proven difficult to constrain due to the heterogeneity of the venting (Barreyre et al., 2012). However, the diffuse heat flux writes:

$$Q_{ad} = S\rho\Delta T v C_p \tag{5}$$

where S is the surface area of the diffuse outflow, ρ is the density of the hydrothermal fluids, ΔT is the temperature difference between the emitted hydrothermal fluids and ambient seawater, v is the velocity of the hydrothermal fluids at the substratum level and C_p is the specific heat capacity of the hydrothermal fluids (Barreyre et al., 2012).

The conductive heat flux through the sediments can be expressed with Fourier's law as:

$$Q_c = -k\nabla T S \tag{6}$$

where $-k$ is the thermal conductivity of the seafloor, ∇T is the temperature gradient and S is the surface area .

Considering the above equations, the parameters needed to constrain the heat flux of LCHF are listed in table 1:

Parameter	Denotation	Unit
Radius of black smoker orifices	r	m
Number of vents	$nVents$	1
Surface area of diffuse venting	S_d	m^2
Velocity of hydrothermal outflow	V_d	$m * s^{-1}$
Heat capacity of hydrothermal fluids	C_{pd}	$J * C^{-1}$
Density of hydrothermal fluids	ρ	$kg * m^{-3}$
Temperature difference	ΔT_d	$°C$
Conductivity of seafloor	k	$W * (m * k)^{-1}$
Temperature gradient of sediments	∇T_c	$C * m^{-1}$
Surface area of conduction	S_c	m^2

Table 1: Parameters needed to constrain the advective and conductive heat flux at the LCHF.

Bischoff and Rosenbauer (1985) derived an empirical equation of state for hydrothermal seawater where the specific heat capacity (C_p) and density (ρ) can be calculated from the temperature of the hydrothermal fluids and the pressure. As the LCHF is situated at a depth of ∼2300 m, the pressure is estimated to be ∼230 bar. The temperature data collected therefore yields the temperature parameters needed ($\Delta T_d, \nabla T_c$), as well as the heat capacity (C_p) and density of the fluids (ρ) (Bischoff and Rosenbauer, 1985). In addition, Sarrazin et al. (2009) proved a strong correlation between the velocity and temperature of emitted diffuse hydrothermal fluids, which means that V_d also can be extrapolated from the temperature data through the following equation:

$$v = \frac{11.566\Delta T - 7.8433}{37.6} \tag{7}$$

where v is the substratum velocity of the diffuse, hydrothermal fluids, and ΔT is the measured temperature corrected for ambient seawater temperature. However, hydrothermal cracks do not follow the equation of Sarrazin et al. (2009), instead the equation in figure 11 developed by Barreyre (2013), based on fluids mechanic laboratory experiments, is used to calculate substratum velocities.

One of the clearest manifestation of hydrothermal activity at the LCHF (and at all hydrothermal fields at large) are micro-bacterial mats and hydrothermal deposits associated

with diffuse flow, in addition to high-temperature, black smoker chimneys. These active areas are clearly visible in the photomosaic imagery (e.g. white zones), serving as a proxy for areas of discrete hydrothermal outflow. Thus, digitization of biomarkers and depositional structures associated to low-temperature ($<100°C$) venting allows the surface area of advective diffuse hydrothermal outflow (S_d) to be constrained. Digitization of black smokers through photomosaic imagery and ROV videography allows the spatial distribution of advective focused hydrothermal outflow to be constrained, which integrated with turbulent plume modelling based on velocities from vertical temperature gradients of advective focused hydrothermal fluids, allow the advective focused flux (Q_{af}) to be constrained.

The total conductive surface area S_c is estimated as a circle encompassing all visible structures associated to hydrothermal outflow, with a diameter of $200m^2$.
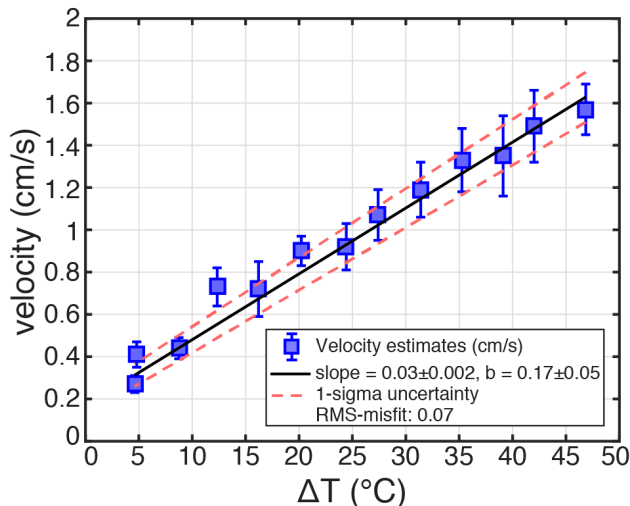
Figure 11: Velocity of substratum hydrothermal fluids of cracks, based on fluid mechanic laboratory experiments. The following equation is $V = 0.03\Delta T + 0.17$, where v is given in cm/s. Courtesy of T. Barreyre.

3.2.2.2 Temperature data

All relevant temperature data were imported in Matlab for further analysis. For the single-point value temperature probes (T-sword, IGTs, GC) the temperature data, probe names and UTM coordinates were imported. IGT samples were generally taken in pairs in the same spots to increase the sample size. Mean temperature data from IGT samples in the same spot were therefore calculated, in addition to a standard deviation of $\pm 1°C$ due to the thermocoupler inaccuracy. The time-series data (from loT, hiT, and hiTT) requires a

different approach. To extract relevant values from these datasets, the mean temperature (T_{mean}) and the standard deviation (σ), were calculated. Time series datasets were also cropped to select only the time when the sensor was deployed in the hydrothermal outflow and therefore discard the time before deployment and after recovery for which the sensor was measuring ambient temperature either in the water column or on the boat.

Digitization of all visible structures associated with hydrothermal venting, in addition to the marking of all temperature probes in Mosaicviewer, provides a way to further categorize temperature data according to which structures they were deployed in. Reference values were then created for each type of digitized structure to constrain the heat flux per type of hydrothermal outflow.

3.2.2.3 Vertical temperature gradient of black smoker plumes

To estimate the volume and heat flux of black smokers at the Loki site, we calculate the shape, centerline upward velocity, and temperature in a hydrothermal turbulent plume ("smoker") as a function of height above the vent, based on classical turbulent plume theory (Morton et al., 1956; Speer and Rona, 1989) using a tabulated equation of state for hydrothermal fluids (Bischoff and Rosenbauer, 1985) and the turbulent entrainment model of Carazzo et al. (2008). We fit the semi-analytical model outputs to the temperature measured by the gradient board inside the plume. Further details on the approach are discussed by Mittelstaedt et al., 2012.

4 Results

4.1 Types of active hydrothermal outflow and distribution

A total of seven distinct types of biomarkers and hydrothermal deposits (referred to as structures from here on) were identified as proxies for hydrothermal outflow and digitized using the processed photomosaics. The types of digitized structures are as follows:

Patches: irregularly shaped, discrete areas of seafloor that display a more or less continuous white surface throughout, with no apparent hydrothermally constructed feature associated (fig. 15). The size of each individual patch is highly variable, and the diameter varies from a few centimeters (limited by resolution of photomosaics) to several meters, with an average and median area of respectively $\sim 0.068\text{m}^2$ and $\sim 0.014\text{m}^2$.

Cracks: discrete, well-defined fissures in the seafloor with a more or less continuous white surface throughout (fig. 16). Each crack typically have a length of ∼1-2 meters, with a low width/length-ratio (typically ∼1/10). The mean surface area digitized cracks are 0.109m^2, and the median surface area is 0.028m^2, showing a large variability in size.

Barite chimneys: discrete, irregularly shaped, three-dimensional structures that show a white, continuous surface throughout (fig. 17). Each barite chimney structure area ranges from a few millimeters (limited by resolution of photomosaic) to ∼1.7m^2, with a mean area of 0.056m^2 and a median area of 0.020m^2, indicating the presence of large clusters of barite chimneys increasing the mean surface area. Each large cluster consists of several barite chimneys coupled by white, regular surfaces, while the smaller digitized barite chimneys consist of discrete chimneys.

Barite flanges: discrete, three-dimensional structures similar to barite chimneys, but distinct in the concentric shape and regular orientation of flanges (fig. 18). Most flanges have a diameter of ∼0.1-0.2 meters, while several clusters of barite flanges, coupled by white, regular surfaces, are digitized with a surface area of 0.4m^2.

Tube Worms: highly irregularly shaped colonies of tube worms (*Sclerolinum contortum* (Pedersen, Rapp, et al., 2010)), with diameters ranging from less than a meter to tens of meters (fig. 19). Some tube worm colonies encompass other structures (e.g. patches, barite chimneys), which are digitized as separate structures if they are clearly distinguishable from the tube worm colonies.

Mounds: two broad sulfide mounds are clearly visible in the photomosaic, elevated above the surrounding seafloor. Each sulfide mound have distinct, continuous white areas around the peak, digitized as mounds (fig. 20).

Black smokers: orifices of advective, focused high-temperature venting (fig. 21). In the photomosaics only one black smoker is visible as the ROV did not move directly above most black smoker chimneys during the photomosaic surveys. Thus, remaining black smoker orifices were digitized using ROV videography to account for the missing orifices. All black smokers were digitized as one-dimensional points, but in reality the black smokers are circular orifices, several centimeters wide (figure 9).

All digitized features, with the exception of black smokers, are digitized as polygons, from which the area of active hydrothermal outflow is estimated.

The most numerous of the identified structures are patches with a total number of 4071 digitized, making up 78% of all digitized structures in the LCHF (Fig. 15). The majority of digitized patches are located in the barite field and areas around black smokers (fig. 12). Patches are white, mottled areas of micro-bacterial mats easily identifiable in the photomosaic.

A total of 967 barite chimneys were digitized, making up 18.5% of all digitized structures (fig. 22). Barite chimneys in the LCHF are exclusively located in the barite field, in a ∼20x30m area. The barite chimneys are finger-like structure composed of barite-silica, several cm tall, covered in white micro-bacterial mats.

Barite "flanges" (Fig. 14) are similiar to barite chimneys, though the shape is the major distinction. While barite chimneys are finger-like structures, barite flanges are flat, concentric structures that are oriented at an angle from the seafloor (fig. 14). All barite "flanges" are oriented in the same direction (∼45°), which might be a result of the orientation of the local deep-sea bottom currents. Barite "flanges" show growth rims, similarly to stromatolites, and are exclusively situated in a small area (∼5x5m) of the barite field. No samples of barite flanges has been collected at the time of this thesis, so any compositional difference between barite chimneys and and barite flanges is currently unknown.

Although tube worm colonies only make up 71 of the digitized structures, each individual patch cover a larger area than all other structures except the inner and outer mounds (Fig. 19). In the photomosaics tube worms are found exclusively in the barite field and oasis, and consist of bacterial mats covered tube worm colonies, or tube worm colonies with no visible underlying biomarkers.

"Mounds" (fig. 20) are the central parts of the sulfide mounds hosting the black smokers. These structures display diffuse venting across their flanks, which are extensively covered by bacterial mats and hydrothermal deposits. A total of two mounds were digitized; one surrounding Sleepy, Menorah and Camel, and one surrounding João. Each mound were sub-divided into two structures: the inner and outer mound. The inner mound encompasses the black smokers, consisting of high-temperature sulfide chimneys with active focused venting. The outer mound is the larger surrounding area (∼5-15m diameter), consisting of debris from the collapsed chimneys, and bacterial mats and hydrothermal deposits indicating extensive diffuse venting, with no visible focused hydrothermal venting.

Orifices of focused venting are marked as "Black Smokers" in the photomosaics, with a total of 14 orifices marked. Sleepy contains one, Menorah contains two, Camel contains four, and João contains seven. Velocities and heat fluxes of high-temperature, focused venting are constrained through through turbulent plume modeling constrained by the plume temperature fields .

All digitized structures were further uploaded and analyzed in Matlab to calculate the surface area of each distinct structure type (fig. 12) for integration into equation 4, alongside temperature data (fig. 13) to constrain the advective, diffuse heat flux.
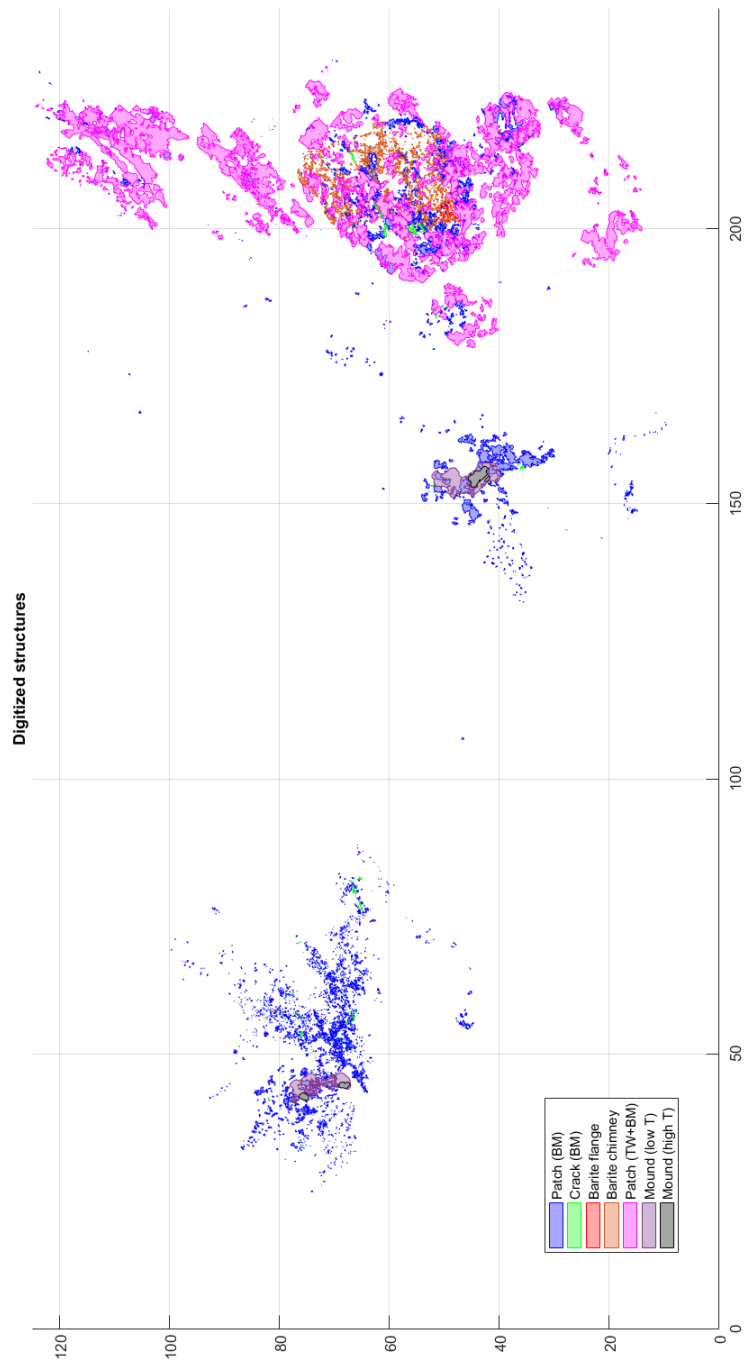
Figure 12: All digitized structures associated with advective, diffuse hydrothermal outflow. Each region (western mound, João, barite field and oasis) is clearly visible here, and their compositional differences. The most complex area is the barite field, containing all classes of structures, except inner and outer mound, and complex associations between them.
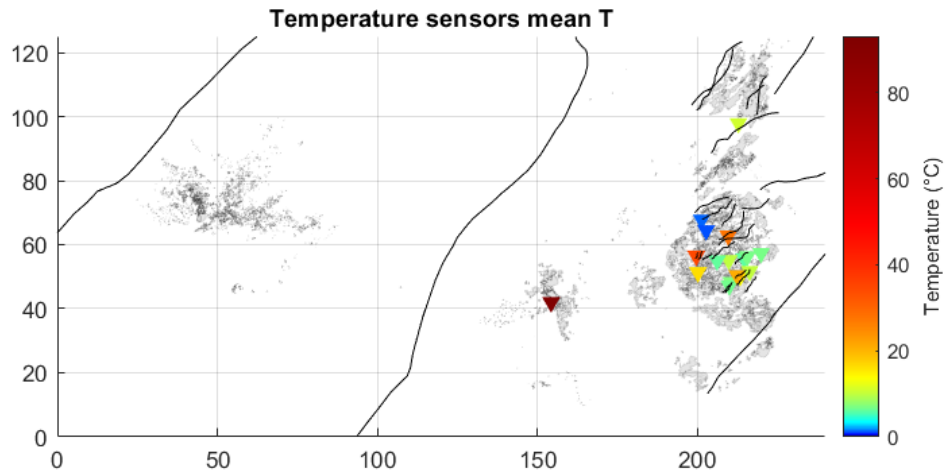
Figure 13: All digitized structures (grey) and fault lineations running through the LCHF digitized from bathymetry data (black lines). All temperature measurements in structures associated to advective, diffuse outflow are marked as triangles, with the color corresponding to the measured temperature
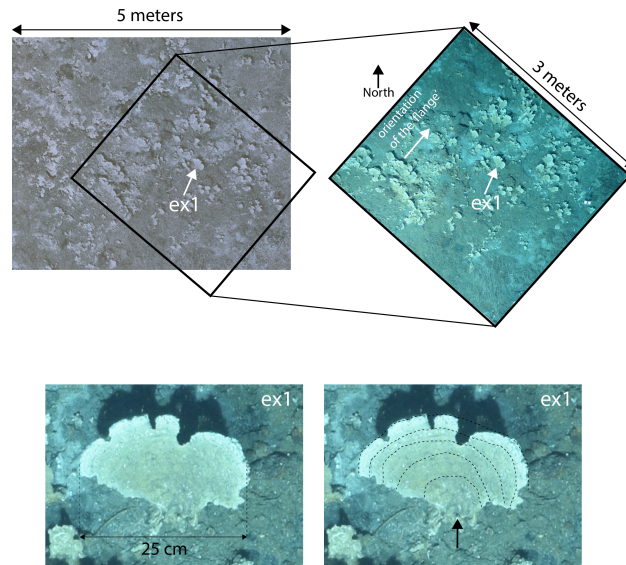
Figure 14: Barite flanges situated in the Barite field. The flanges seem to grow concentrically to the northwest. No flange sample has been collected at the time of this thesis, so the composition is unknown.

Figure 15: Example of structures categorized as "patch". (A) A raw image captured during photomosaic survey GS18_218_ROV30 with the arrow showing the heading of the ROV in (B) and the dotted line marking the edge of a diffuse micro-bacterial patch. (B) ROV footage showing the same area of diffuse venting. (C) Post-processed, pre-digitized photomosaic imagery with arrow marking the ROV heading in (B). (D) Digitized photomosaic imagery of the same area of diffuse venting. "Patches" are marked as 2D_p in (D), with a blue outline.

Figure 16: Example of a structure categorized as "crack". (A) Raw image captured during photomosaic survey GS18_218_ROV30 with the arrow showing the heading of the ROV in (B) and the dotted line marking the edge of a diffuse bacterial crack. (B) ROV footage showing the same area of diffuse venting. (C) Post-processed, pre-digitized photomosaic imagery with arrow marking the ROV heading in (B). (D) Digitized photomosaic imagery of the same area of diffuse venting. "Cracks" are marked as 2D_cr in (D), with a green outline.

Figure 17: Example of a structure categorized as "barite chimney". (A) Raw image captured during photomosaic survey GS18_218_ROV30 with the arrow showing the heading of the ROV in (B). (B) ROV footage showing the same area of diffuse venting. (C) Post-processed, pre-digitized photomosaic imagery with arrow marking the ROV heading in (B). (D) Digitized photomosaic imagery of the same area of diffuse venting. Barite chimneys are marked as 3D_p in (D), with a orange outline.
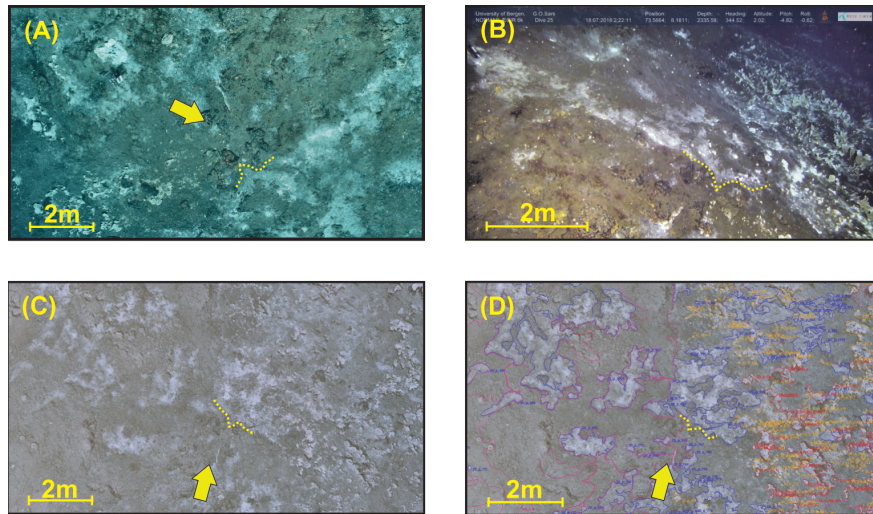

Figure 18: Example of a structure categorized as "barite flange". (A) Raw image captured during photomosaic survey GS18_218_ROV30 with the arrow showing the heading of the ROV in (B). (B) ROV footage showing the same area of diffuse venting. (C) Post-processed, pre-digitized photomosaic imagery with arrow marking the ROV heading in (B). (D) Digitized photomosaic imagery of the same area of diffuse venting. Barite flanges are marked as 3D_p_fin in (D), with a red outline.
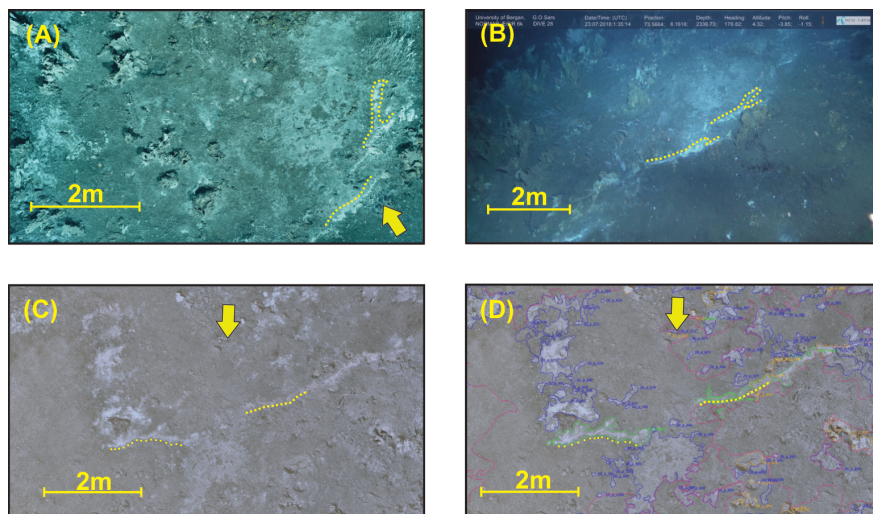
Figure 19: Example of a structure categorized as "tube worms". (A) Raw image captured during photomosaic survey GS18_218_ROV30 with the arrow showing the heading of the ROV in (B) and the dotted line marking the edge of a digitized colony of tube worms. (B) ROV footage showing the same area of diffuse venting. (C) Post-processed, pre-digitized photomosaic imagery with arrow marking the ROV heading in (B). (D) Digitized photomosaic imagery of the same area of diffuse venting. Tube worms are marked as TW in (D), with a purple outline.
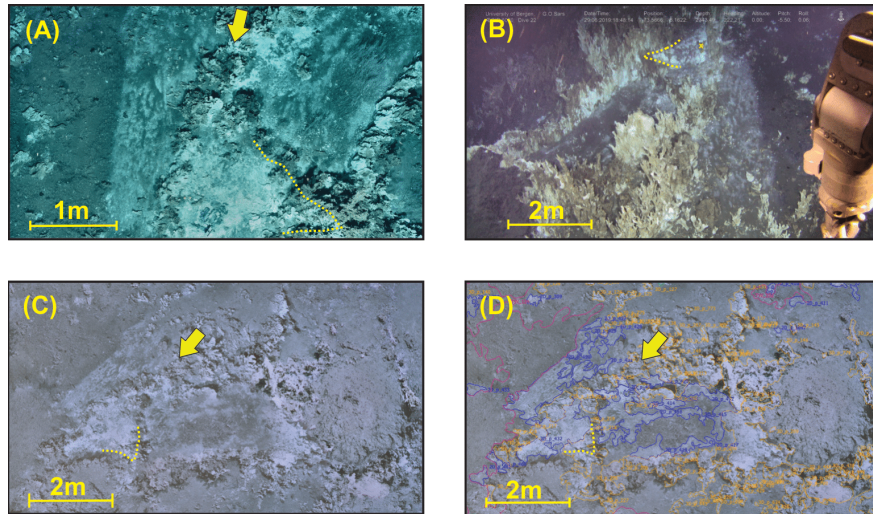

Figure 20: Example of a structure categorized as "mound". (A) Raw image captured during photomosaic survey GS18_218_ROV31 with the arrow showing the heading of the ROV in (B). (B) ROV footage showing the same area of venting. (C) Processed, pre-digitized photomosaic imagery with arrow marking the ROV heading in (B). (D) Digitized photomosaic imagery of the same area of diffuse venting. Mound is marked as mound in (D), with an orange outline.
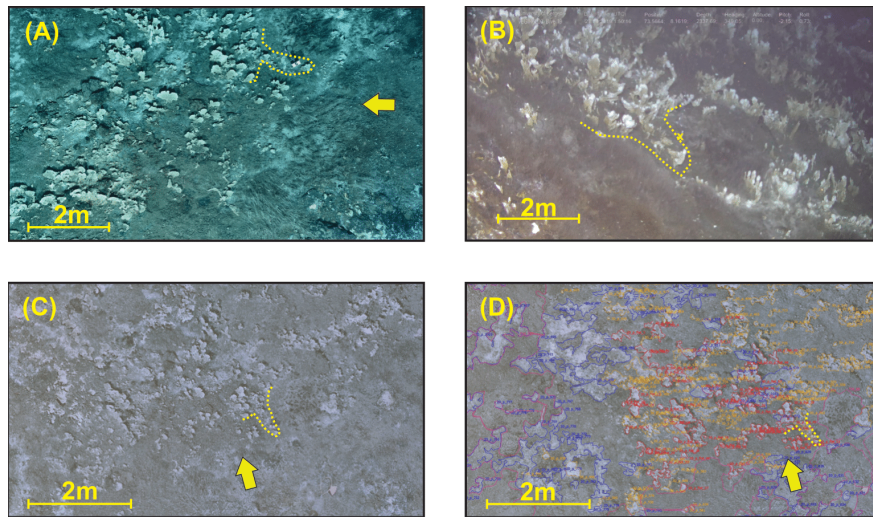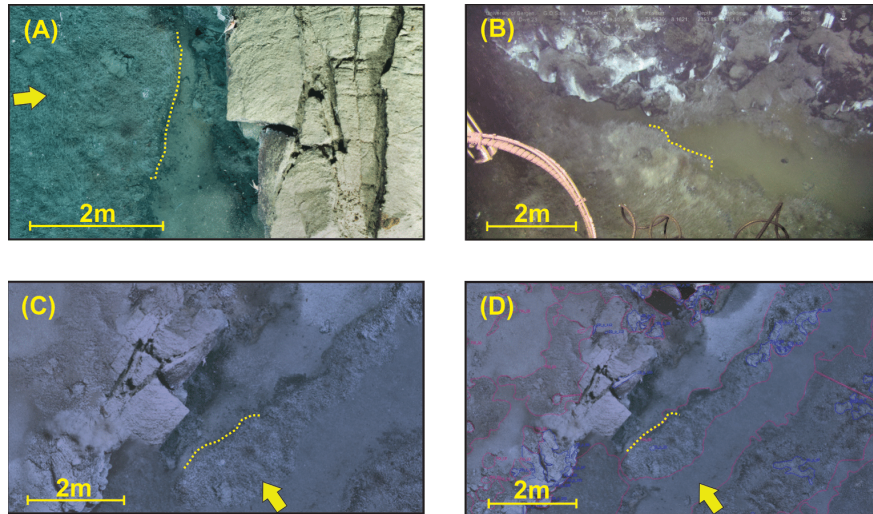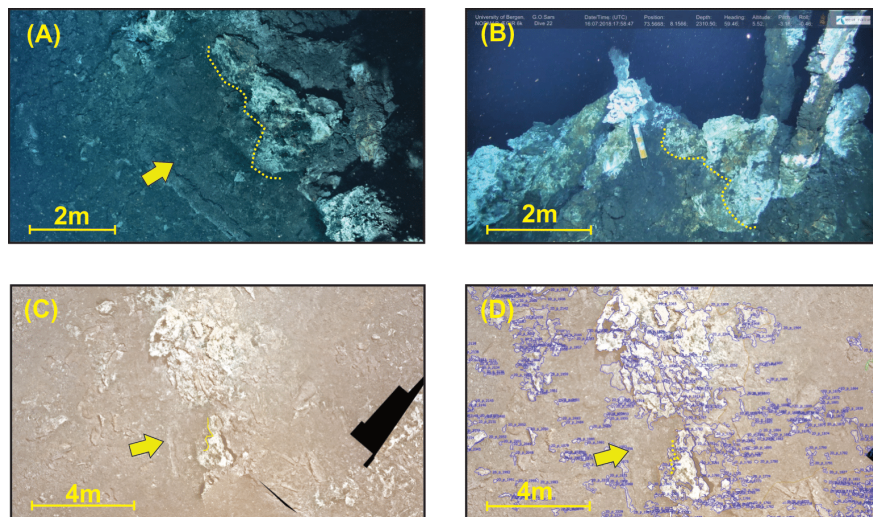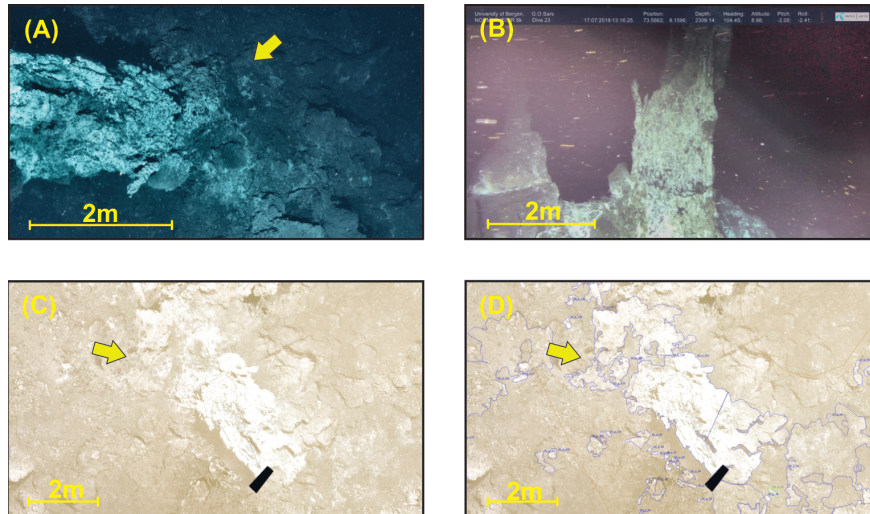
Figure 21: Example of a structure categorized as "Inner mound". The chimney itself is the type "inner mound", while the orifices of high-temperature, focused venting are marked as "black smokers" in the photomosaic. (A) Raw image captured during photomosaic survey GS18_218_ROV30 with the arrow showing the heading of the ROV in (B). (B) ROV footage showing the same area of diffuse and focused venting. (C) Post-processed, pre-digitized photomosaic imagery with arrow marking the ROV heading in (B). (D) Digitized photomosaic imagery of the same area of venting. Note how no orifice of the chimney is visible in the photomosaic as the ROV did not fly directly above the black smoker during the survey.

4.2 Surface area (S) of diffuse hydrothermal outflow

Digitization of diffuse, hydrothermal structures in Mosaicviewer and further processing in Matlab provides constraints on the surface area of all hydrothermal structures (Table 2) in addition to the number of structures digitized. As some of the digitized structures overlap partially or completely, the surface area was corrected by creating a hierarchy of diffuse outflow structures according to the associated temperature measurements, with the warmer structures (e.g. inner mound) being prioritized over cooler structures (e.g. tube worms) (fig. 23), and subtracting area of overlap from the cooler structures when applicable (table 3).

Overall, the surface area calculated here is likely a minimum estimate, first due to the fact that some active areas may have not been imaged or identified. Second, additional hydrothermal activity may be present beyond the surveyed areas. Systematic searches and transits in successive cruises have yielded no additional active vents, suggesting that the extent of active venting at the Loki vent field is well-define. Third, due to the inherent projection of the orthomosaic, the estimated surface area does not account for the three-dimensional nature of certain structures (e.g. mounds, barite chimneys), resulting in calculated surface

area that is lower than the surface area of the actual structures.

	BF	Oasis	João	L.E. remaining	Loki west	Total	Number of digitized structures
Cracks	3.67	0	0.45	0.27	1.18	5.57	52
Patches	105.92	14.28	61.69	6.23	73.67	261.79	4171
Tube worms	467.03	164.74	0	70.94	0	702.71	71
Barite flange	1.92	0	0	0	0	1.91	56
Barite chimney	53.79	0	0	0	0	53,79	967
Inner mound	0	0	7.3	0	3.49	10.78	3
Outer mound	0	0	17.19	0	15.84	33.04	2
Total	632.33	179.02	86.93	77.43	94.18	**1069.60**	5220

Table 2: Total surface area of each type of digitized structure after correcting for overlap, classified by zone. All values, except the number of digitized structures, are given in m^2.

	Patches	Tube worms	Crack	Barite chimneys	Barite flanges	Inner mound	Outer mound	Total
Patches	NaN	27.33	0.001	0.06	0.001	8.20	31.95	67.54
Tube worms	27.33	NaN	0.13	0.30	0.001	0	0	27.76
Cracks	0.001	0.13	NaN	0.08	0	0	0.11	0.33
Barite chimneys	0.06	0.30	0.08	NaN	0.001	0	0	0.45
Barite flanges	0.001	0.001	0	0.001	NaN	0	0	0.003
Inner mound	8.20	0	0	0	0	NaN	10.78	18.99
Outer mound	31.95	0	0.11	0	0	10.78	NaN	42.84
Total	67.54	27.76	0.33	0.45	0.003	18.99	42.84	**157.91**

Table 3: Overlapping area between each type of digitized structures. Each value is given in m^2. Areas listed here were subtracted from the calculated area of relevant patches (e.g. overlap between tube worms and cracks were subtracted from the calculated surface area of cracks).

4.3 Temperature (T)

4.3.1 Diffuse flow

For all classes of digitized structures associated with diffuse hydrothermal outflow temperature data was collected, except for *barite chimneys* and *barite flanges*. Although no temperature sensors were deployed in the barite structures themselves, temperatures were measured in the bacterial mats at the base of several barite chimneys (Fig. 22). White bacterial mats hosted on the surface of barite structures are similar to the bacterial mats digitized as *patches*, and the mean temperature of sensors deployed at the base of barite structures are comparable to the measured mean temperature of *patches* (6.0-10.2°C vs. 6.9-13.6°C). Therefore the barite structures (*barite chimneys* and *barite flanges*) are grouped together with the *patches* as a single group for the temperature values, namely *patches (BM)* where BM is an abbreviation for bacterial mats. Each mound and associated black smoker chimneys were divided in two categories: the inner and outer mound. The inner mound is the black smoker chimney itself and the part of the mound hosting the black smokers, while the outer mound is the surrounding area of the mound where bacterial mats associated to diffuse outflow grow on the flanks. To get a conservative heat flux estimate of the mounds, the temperature data collected from *patches (BM)* were integrated in the outer mound area as the outer mound is covered by bacterial mats. As tube worm patches generally also consist of bacterial mats, this category is named *patches (TW + BM)* to indicate the presence of both tube worms and bacterial mats, although the measured temperature of these areas differ from the *patches (BM)* values.

Figure 22: Example of a barite chimney. Temperature data were collected by deploying a hiT sensor (GS18_hiT21) in the white bacterial patch at the base of the chimney. The chimney itself is covered by mottled bacterial mats similar to the digitized class *patch (BM)*.

All mean temperatures and standard deviations were sorted by structures (*patches (BM)*, *patches (TW + BM)*, *cracks (BM)* and *inner mound*) to extract a range of reference temperatures used to constrain the advective diffuse heat flux (fig. 23). The minimum and maximum temperatures were also extracted from each temperature sensor to find the minimum and maximum potential diffuse heat flux of the LCHF.
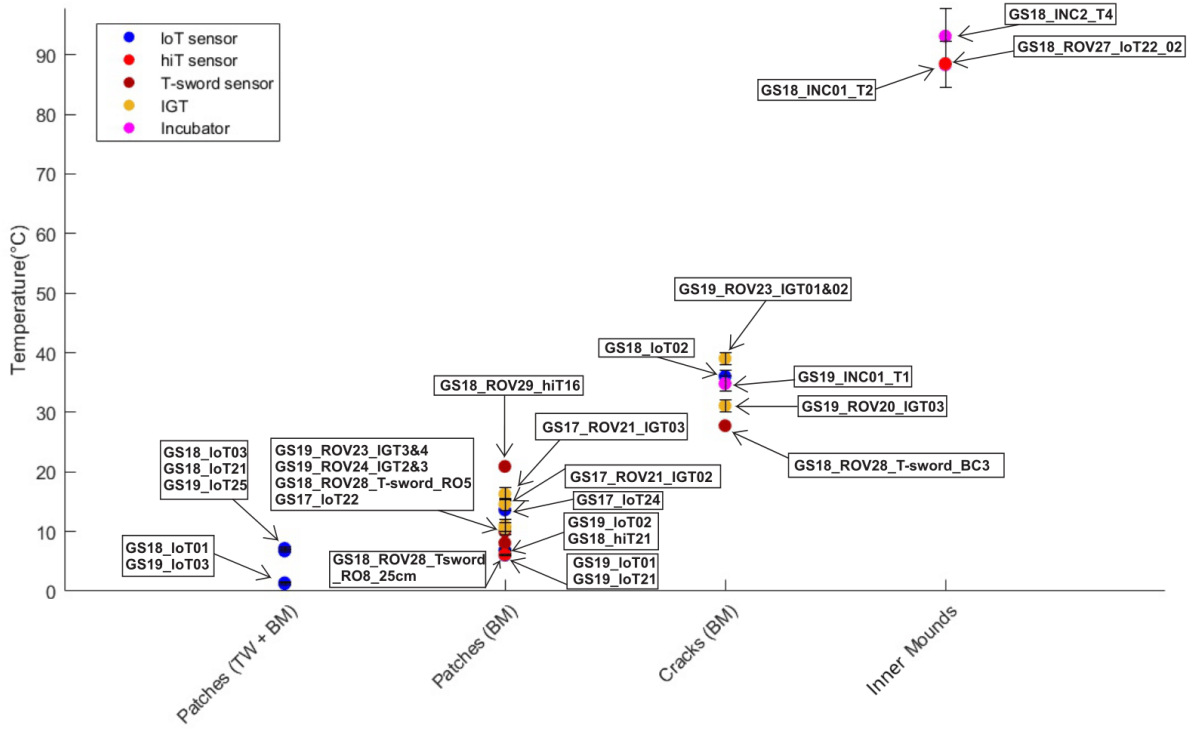
Figure 23: All mean temperatures used in this thesis grouped by structure in which the data were collected. All temperature values extracted from time series were plotted with the standard deviation ($+\text{-}\sigma$), while single point temperature measurements were plotted without a standard deviation value.

4.3.2 Focused flow

High-temperature probes were deployed in all four black smoker chimney at various time intervals through 2017-2019. All sensors were left recording over the course of $\sim$one year, resulting in time-series of temperature data. The maximum measured temperature is used as an analogy for unadulterated, circulating hydrothermal fluids, which can be used to calculate the mass-, volumetric- and chemical fluxes (described in the discussion chapter).

4.4 Velocity (V) of diffuse flow

Exit-fluid velocities of all digitized structures associated with diffuse outflow, except *cracks*, were calculated following Sarrazin's linear scaling for diffuse patches outflow (eq. 7, Sarrazin et al., 2009). For the diffuse outflow structures *cracks*, the equation in fig. 11 were used (Barreyre, 2013). Velocity ranges for each structure type is given in table 4:

Structure type	Velocity (mm/s)
Patches (TW + BM)	0.39 - 2.21
Patches (BM)	1.86 - 6.44
Cracks	10.03 - 13.42
Mound	27.18 - 28.65

Table 4: Substratum velocities of diffuse hydrothermal fluids calculated from measured mean temperatures.

4.5   Thermal gradients in background sediments

From the three gravity core samples collected with temperature probes attached to the outer cylinder, temperature data was extracted and corrected for equilibrium time. By applying a linear regression function the temperature gradient (∇T) of the background sediments at the LCHF was calculated (table 5). From the world heat data (Jessop et al., 1975), the thermal conductivity (k) of the sediments was extracted (table 5).

Sample name name	Latitude	Longitude	Thermal gradient (°C/m)	Thermal conductivity (W/m°C)
GS19_GC17	73.56648	8.159167	-0.42339	1.01±0.06
GS19_GC19	73.56615	8.1616	-0.55664	1.14±0.06
GS19_GC20	73.56711	8.15795	-1.047	1.14±0.06

Table 5: Sample names and ship location of each gravity core sample included in this thesis. Thermal gradients and thermal conductivity shows the constrained values for each GC location.
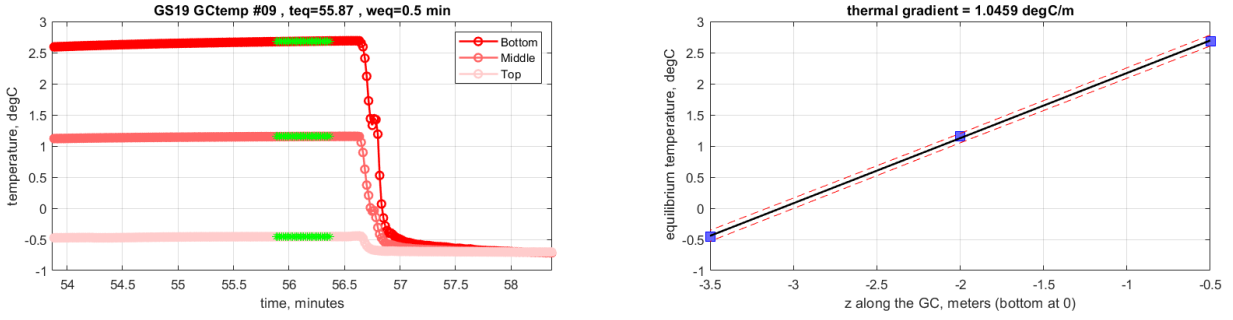
Figure 24: Temperature data and results from gravity core sample GS19_GC09. **Left:** temperature data at equilirium recorded by GC09, from all three temperature sensors. Green segments mark the time and value of temperature data used for linear regression calculations. **Right:** thermal gradient calculated through linear regression, with blue squares marking the temperature values used. The slope gives the vertical thermal gradient of the sediments, and the dashed red line is the standard deviation.

4.6 Heat fluxes (Q)

4.6.1 Advective heat flux (Q_a)

4.6.1.1 diffuse (Q_{ad}) - by structure

To constrain the advective diffuse heat flux, each digitized structure may be treated in regard to its classification - disregarding spatial distribution. The heat flux of each digitized structure is therefore shape-dependant, where the shape (f) is the type of digitized structure (e.g. patch (BM), crack). Due to the non-linear dependence of C_p and ρ to T, each parameter in equation (5), except S, were calculated as a vector of the same length as the number of temperature measurements (fig. 23) for a given structure type (e.g. Patches (TW+MB), cracks (BM)), resulting in equation (5) being rewritten as:

$$
\begin{bmatrix} HF_1 \\ . \\ . \\ . \\ HF_{n-1} \\ HF_n \end{bmatrix} = \begin{bmatrix} \Delta\text{T}_1 \\ . \\ . \\ . \\ \Delta\text{T}_{n-1} \\ \Delta\text{T}_n \end{bmatrix} * \begin{bmatrix} v_1 \\ . \\ . \\ . \\ v_{n-1} \\ v_n \end{bmatrix} * \begin{bmatrix} \rho_1 \\ . \\ . \\ . \\ \rho_{n-1} \\ \rho_n \end{bmatrix} * \begin{bmatrix} C_{p1} \\ . \\ . \\ . \\ C_{pn-1} \\ C_{pn} \end{bmatrix} \tag{8}
$$

where HF is the diffuse heat flux per square meter (Q_{ad}/S) for the type of digitized structure,

and n is the number of temperature measurements for the structure type (fig. 23, table 6). *HF* were used in further calculations, with a range of values corresponding to each type of digitized structure (fig. 25). The total heat flux Q_{ad} for the type of structure is then written as:

$$
\begin{bmatrix}
Q_{ad1} \\
. \\
. \\
. \\
Q_{adn-1} \\
Q_{adn}
\end{bmatrix}
=
\begin{bmatrix}
HF_1 \\
. \\
. \\
. \\
HF_{n-1} \\
HF_n
\end{bmatrix}
* S
\tag{9}
$$

All values for the total advective, diffuse heat flux (Q_{ad}) were then calculated to constrain the minimum-, maximum- and mean advective heat flux (table 9) from parameters listed in table 7. The pressure (p) is assumed to be constant across the entire LCHF, although in reality the pressure varies as a function of depth and density of the overlying seawater. The shape factor (f) is the type of digitized structure, although only the exit-velocity calculation is shape-dependant, as the equation used depends on whether the structure is a crack or not. Parameters ΔT, v, ρ and C_p were calculated as vectors the same length as n for each type of digitized structure.

	Patch (TW + BM)	Patch (BM)	Crack (BM)	Mound
n	5	13	5	3

Table 6: Number of temperature measurements for each type of digitized structure, as shown in fig. 23.

Denotation:	Function of:
ΔT	(T_{measured})
v	$(\Delta T, f)$
ρ	$(\Delta T, P)$
C_p	$(\Delta T, P)$

Table 7: Values used to calculate parameter in equation 5.
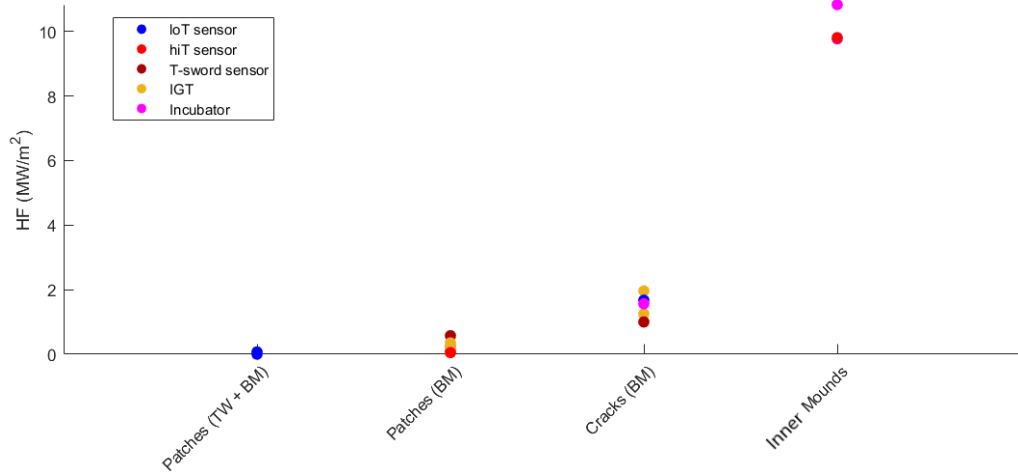
Figure 25: Range of heat fluxes Q/S for each type of structure, calculated from the mean temperature of each deployed temperature sensor.

	Mean Q_{ad} (MW)	Min. Q_{ad} (MW)	Max. Q_{ad} (MW)
Cracks	9.594	6.6759	12.3782
Patches	47.8332	13.5635	150.1377
Tube Worms	29.6497	2.2079	50.7102
Barite chimneys	9.8322	2.788	30.8612
Barite flanges	0.3549	0.1006	1.114
Outer mound	7.5377	2.1374	23.659
Inner mound	114.0652	110.0876	121.6202
Total	**219**	**138**	**390**

Table 8: Total advective, diffuse heat flux of the Loki's Castle hydrothermal field sorted by structure type.

4.6.1.2 diffuse (Q_{ad}) - by zone

Digitization of faults running through the LCHF from bathymetry data, in combination with temperature data, reveal possible fault-controlled zones emitting fluids of compareable temperatures within each zone (fig. 26 bottom). The advective diffuse heat flux may be constrained in regard to the digitized fault-zones using the average measured temperature in the area, while constraining fluxes of all excluded structures in the same method as described in paragraph *diffuse (Q_{ad}) - by structure*.

Distribution of temperature data collected in the barite field reveal temperature measurements within certain zones to have similiar values, even though the structure type in which the measurements are done differ (fig. 26 bottom). Three temperature zones were therefore created, implying the faults at the LCHF act as a plumbing system for the advective diffuse hydrothermal outflow in the barite field.

All fluxes were calculated in the same manner as described above, integrating surface areas and temperature values in equation 5 to constrain Q_{ad}. For the barite field zones (fig. 26) the mean of all measured temperatures within the zones, as well as the combined surface area of all digitized structures within the zones, were used to constrain Q_{ad}.

	Mean Q_{ad} (MW)	Min. Q_{ad} (MW)	Max. Q_{ad} (MW)
Zone A	0.1741	0.1423	0.2090
Zone B	77.6013	69.3457	86.3162
Zone C	12.5914	11.5045	13.7272
Excluded structures	188.967	127.2957	313.8998
Total	**279**	**208**	**414**

Table 9: Total advective, diffuse heat flux of the Loki's Castle hydrothermal field sorted by structure type, assuming that fault-controlled temperature zones exist in the barite field.
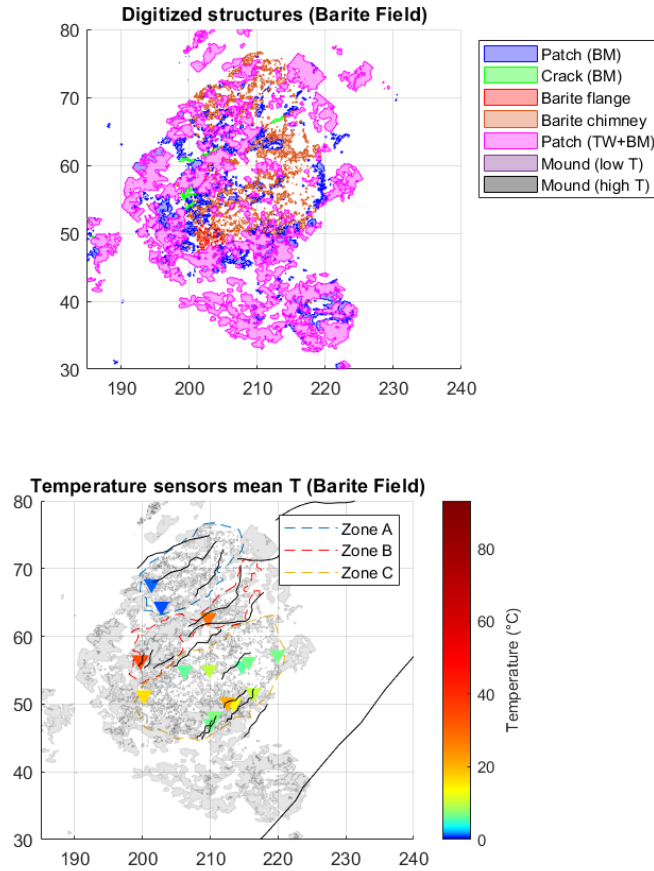
Figure 26: Top: All digitized structures in the Barite field.
Bottom: All digitized structures in the Barite Field are marked in grey, while the black streaks show the faults running through the Barite Field (digitized from bathymetry data). Markers show all temperature measurements in structures associated with diffuse hydrothermal outflow, color coded by measured temperature. Temperature zones are marked in dashed lines.

4.6.1.3   Focused (Q_{af})

The temperature values extracted from the gradient board were chosen based on the time of the highest temperature-variations (fig. 27 a) to constrain the maximum focused heat flux (Q_{af}), minimizing thermal influence from surrounding seawater. All measured temperature values were further processed as ranges (instead of single-point measurements) to account for any errors (fig. 27 b). The semi-analytical model described in paragraph 3.2.2.3 were then applied to the measured temperatures, resulting in a focused heat flux per vent (Q_{af}/V) equal to 0.8MW $\pm$0.2MW (fig. 27 c). Multiplying this constraint by the number of vents

provides a range of total focused heat flux: $Q_{af} = 11.2\text{MW} \pm 2.8\text{MW}$
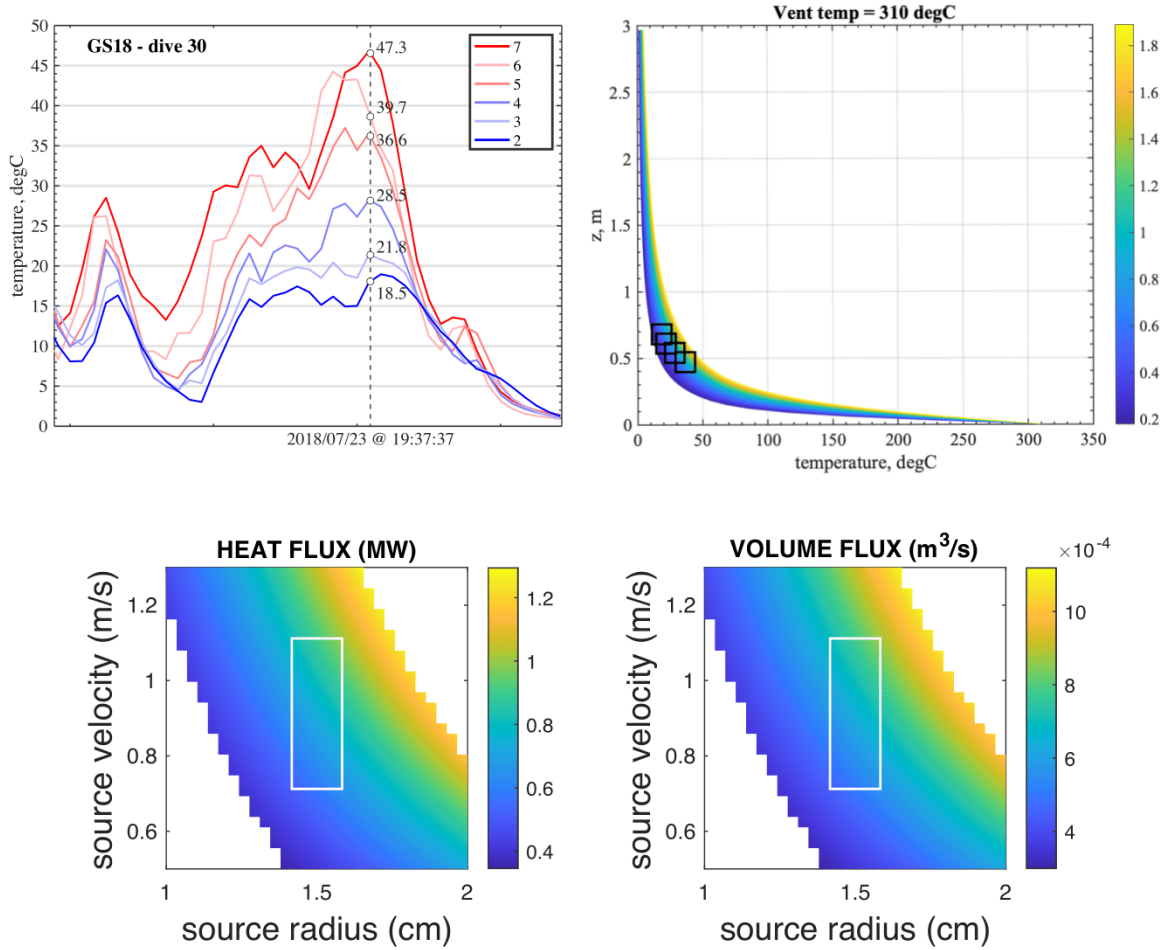
Figure 27: Top left: Measured temperature from all seven probes in the gradient board. The lowest temperature (sensor 2) was measured by the sensor at a highest vertical distance of the orifice. Sensor 1 malfunctioned prior to the measurements. **Top right:** measured temperature plotted in regards to the vertical distance to the vent, from which the heat flux is modeled. The black boxes mark the temperature ranges, accounting for positioning errors (on z) above the orifice and sensor logger errors. **Bottom left:** exit-fluids velocities and radius of the orifice modeled for the same heat flux constraints ans presented in the top right. **Bottom right:** associated volume flux of the emitted fluids, calculated through the equation of state for hydrothermal seawater (Bischoff and Rosenbauer, 1985) and heat flux estimate.

4.6.2 Conductive heat flux (Q_c)

Integration of the calculated thermal conductivity and thermal gradient (table 5) into Fourier's equation of conductive heat loss (eq. 6) results in the calculated conductive heat flux for each GC location (table 10). Because of the great depth of the LCHF, any slight angular dis-

placement of the wire connecting the gravity corer to the ship will result in a non-negligible displacement of the gravity core location on the seafloor relative to the ship (fig. 28). An angle of 1°leads to an error circle with a diameter of 84 meters, encompassing all GC local-tions. Therefore the mean of the three heat fluxes is used to calculate the total conductive heat flux (Q_c) as a constant value with no spatial variability, instead of a decreasing function of distance to the heat source. The total area of conductive heat flux was set to be a circle encompassing all digitized structures in the photomosaics, with a diameter of 200m. By integrating all the parameters of table 5 in Fourier's law (eq. 6), the resulting conductive heat flux (Q_c) is estimated to be 0.0242 ± 0.0013 MW (table 10).

Sample	Mean Q_c (MW)	Min. Q_c (MW)	Max. Q_c (MW)
GS19_GC17	0.0152	0.0144	0.0160
GS19_GC19	0.0199	0.0189	0.0210
GS19_GC20	0.0375	0.0355	0.0395
Mean	0.0242	0.0229	0.0255

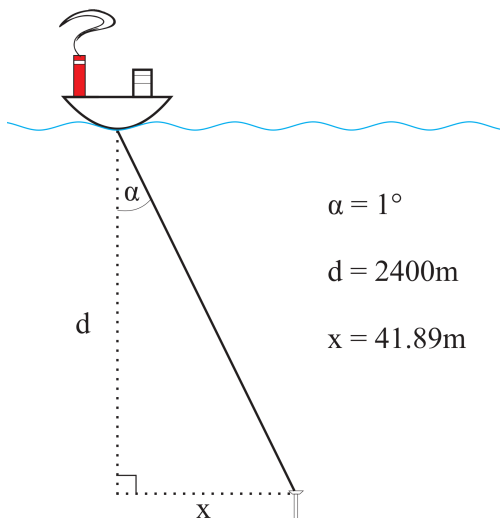**Table 10:** Total conductive heat flux through sediments at the LCHF.

Figure 28: Sea currents, the Coriolis and inertial intristic GC swing effect might cause an angular offset between the ship and GC wire, resulting in a ~42m geographical offset for each degree. For reference the LCHF is ~ 150x200m, resulting in a precision of <2° needed to be certain the sampler hits the vent field.

4.6.3 Total heat flux (Q_{tot})

The total heat flux is expressed as:

$$Q_{\text{tot}} = Q_{ad} + Q_{af} + Q_c \tag{10}$$

where ranges are constrained for all fluxes. As the advective diffuse heat flux (Q_{ad}) is constrained two times, in regard to the type of digitized structures and in regard to the possible fault-controlled temperature-zones in the barite field (explained in detail in section 7.1.1 *Advective heat flux (Q_a)*), two possible ranges of the total, hydrothermal heat flux at the LCHF are constrained (table. 11).

	Q_{ad} (MW)	Q_{af} (MW)	Q_c (MW)	Total (MW)
min. (no T zones)	137.6	8.4	0.023	**146.02**
max. (no T zones)	390.5	14.0	0.026	**404.53**
mean (no T zones)	218.9	11.2	0.024	**230.12**
min. (T zones)	208.3	8.4	0.023	**216.72**
max. (T zones)	414.2	14.0	0.026	**428.23**
mean (T zones)	279.3	11.2	0.024	**290.52**

Table 11: Total constrained heat flux at the LCHF.

5 Discussion

As hydrothermal fluids are emitted from the seafloor, the buoyant plume rises vertically in the water column until it reaches a height of neutral buoyancy, where the fluid then disperses horizontally (and under forcing of currents currents). One method to constrain the flux is through measurements of hydrothermal "traces" (e.g. chemical or thermal anomalies) in the water column, and from this estimating the heigth of the plume and volume of fluids emitted from the originating hydrothermal field (e.g. Jean-Baptiste et al., 1998, Jean-Baptiste et al., 2004, Lowell et al., 2020). These plume-based methods are inherently imprecise owing to the numerous assumptions required to infer heat fluxes at the seafloor from the measured plume properties (physical, chemical). Another method for constraining the flux is the one used in this thesis, through integration and up-scaling of measurements and constraints on individual vents and areas of hydrothermal outflow (e.g. Cooper et al., 2000, Sarrazin et al.,

1999, Barreyre et al., 2012). While this method provide better constraint on the parameter-scale, they are also subject to important operational constraints in the field (e.g., limited time with inhabited or remotely operated vehicles, partial set of measurements), and therefore important assumptions and extrapolations from point measurements to the whole are thus necessary.

5.1 Estimated Q and partition between focused- and diffuse flow

To constrain the total advective heat flux Q_a of a hydrothermal vent field both the diffuse and focused outflow must be constrained. Estimates of the heat flux carried by diffuse effluent alone range from 0% to 100% of the total axial heat flux and vary depending upon the vent field and the measurement technique (Rona and Trivett, 1992, Schultz et al., 1992, Baker et al., 1993, Ginster et al., 1994, Elderfield and Schultz, 1996, J. S. Stein and Fisher, 2001, Nielsen et al., 2006, Ramondenc et al., 2006, Veirs et al., 2006, German et al., 2010, Mittelstaedt et al., 2012, Barreyre et al., 2012). German et al. (2010) found, based on water column surveys of the non-buoyant plume, that the diffusive partition of the Rainbow Vent Field (located in the southern Mid-Atlantic Ridge) was below their detection limit. On the other end of the scale, constraints placed on the East Pacific Rise by Ramondenc et al. (2006) suggest a heat flux through diffuse hydrothermal fluids 10 to 1000 times the flux through focused fluids.

Parameters used in this thesis are well-constrained, total focused flux (Q_{af}) being the least constrained component, as it is extrapolated from a single measurement. The minimum- and maximum heat flux estimated in this thesis is ∼146 MW and ∼291 MW, with a diffusive partition of ∼90%.

5.1.0.1 Q_{tot} from water column estimated

The water column approach of constraining the heat flux was applied at the Rainbow hydrothermal vent field (RHVF) by Jean-Baptiste et al. (2004), resulting in an estimate of the total hydrothermal output of 1320 ± 600 MW. Due to the similarity of the ^{3}He-profile (the chemical concentration used to extrapolate the heat output) of the LCHF and RHVF, the total heat output was estimated to be the same for the two systems (Stensland, 2013). Constraints placed on the total heat flux through ^{3}He measurements and CTD data, vary greatly from the results in presented in this thesis (720-1920 MW vs. 146-429 MW).

While the total heat flux constraint presented here likely is a minimum estimate due to the calculated surface area likely being lower than the actual surface area of diffuse venting, the surface area not accounted for is unlikely to emit 290-1774 MW of thermal energy. While the method of Jean-Baptiste et al., 2004, through ^{3}He and CTD data, does provide constrains within the same order of magnitude as constraints though photomosaic imagery and integration of temperature measurements, our method provides higher control of each parameter (e.g. surface area of diffuse venting, measured temperature, type of outflow) and better constraints on the partition of the different components of hydrothermal fluxes (Q_{ad}, Q_{af}, Q_c).

5.2 Distribution of the heat fluxes

Through digitization of all biomarkers and hydrothermal deposits at the LCHF, the centroids of each structure were calculated in Matlab, to map the distribution of hydrothermal outflow at the LCHF. Figure 29 show the spatial distribution of digitized structures at the LCHF. Almost exclusively the digitized structures are located in the four regions of interest: the western mound, eastern mound, barite field and oasis. Based on the same principles, the constrained heat flux (Q) were integrated to the map showing distribution of structures. The resulting map (fig. 30) shows distribution of constrained fluxes, where each square is the sum of fluxes withing a 5m by 5m area. Though the "pixel" with the highest interpolated flux ($\sim$84 MW) is situated near João, the majority of the flux thrugh this 5x5m^2 square originates from the inner mound (non-focused black smoker) structure. Approximately $\sim$30% to $\sim$50% of the constrained heat flux at the LCHF are lost through diffusive venting at the inner mounds (black smoker chimneys), indicating a high level of mixing in the chimneys between the high-temperature fluids and seawater. The clustering of hydrothermal structures (fig. 29), and $\sim$30% of the heat flux total heat is lost through the barite field, where fluxes are concentrated in the four regions of interest, is clearly linked to the spatial distribution of fluxed as both figures show the same concentration to the same four zones.
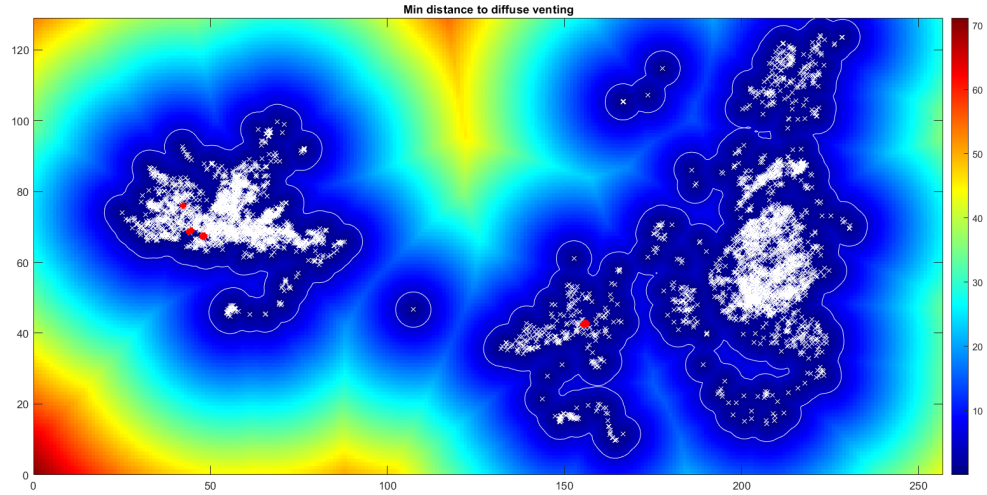
Figure 29: Distribution of all digitized structures at the LCHF. White crosses mark centroids of each structure associated to diffuse venting, and red dots mark high-temperature focused venting. The entire vent field was color coded according to the distance to the nearest digitized structure in meters.
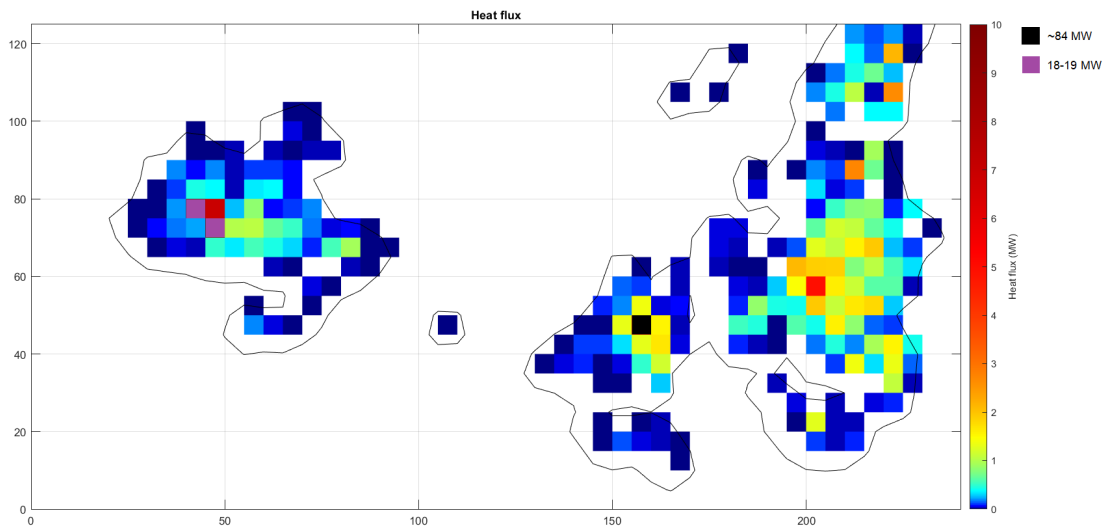
Figure 30: Distribution of constrained heat flux means at the LCHF. Each pixel is a 5x5m square, color coded by the total heat flux emitten in that locality. The values used are the mean heat fluxes (table 11), calculated through the assumption that no temperature zones exist in the barite field.

5.3 Estimation of water mass- and volumetric fluxes

5.3.1 Mass fluxes for hydrothermal fluids

The hydrothermal heat flux (Q) is related to the mass flux of fluids (MF) by the temperature of the emitted fluids (T) and by the heat capacity (C_p) of the emitted fluids:

$$MF = \frac{Q}{C_p T} \tag{11}$$

where Q is the total heat flux (estimated through classification of digitized structures, descibed in detail in paragraph 4.6.1.1 *diffuse (Q_{ad}) - by structure*). Q, T and C_p were constrained with respect to the different types of digitized structures, thus the total diffuse mass flux (M_d) is calculated in the same manner. M_d is then estimated as the sum of all calculated, diffuse mass fluxes. The total diffuse mass flux are presented in table 12. The mean calculated mass flux is 2835 kg/s (table 12).

A range of plausible field-wide hydrothermal mass fluxes through advective, focused venting can be obtained if we assume that to a first order the fluid characteristics do not vary across the site (e.g. temperature and/or ambient pressure). If we assume that all the heat flux may be associated with high-temperature black smoker fluid venting at ∼320°C and ∼230 bar, the focused mass flux M_f may range from 5.14 - 8.57 kg/s (see table 12). The total hydrothermal mass flux (MF_{tot}) of the LCHF, expressed as the sum of diffuse mass flux (M_d) and focused mass flux (M_f) is then 1605.8 - 4683.4 kg/s, with an average values of 2842.1 kg/s. This equation (11) relies heavily on the heat capacity (C_p) of the emitted fluids, which increases significantly as the as the conditions approach the two-phase boundary, especially near the critical point (∼405°C , ∼300 bar), where values are only semi-quantitative (Bischoff and Rosenbauer, 1985). Thus any slight variations in parameters T and P (from which C_p is calculated) will have a great impact on the Q_{ad} constraints.

Using the same parameters used in the MF calculations (eq. 11), in addition to the density (ρ) of emitted hydrothermal fluids, the volumetric flow rate (VF) can be calculated as:

$$VF = \frac{Q}{\rho C_p T} \tag{12}$$

and estimated with respect to each type of digitized structure in the same manner as equation 9. ρ is calculated as a vector through the equation of state for hydrothermal seawater (Bischoff and Rosenbauer, 1985), resulting in a vector the same length as Q, C_p and T for each type of digitized structure. Resulting calculated volumetric flow rates are presented in table 12 for advective diffuse and advective focused hydrothermal outflow.

	Advective diffuse	Advective focused
Q range (MW)	137.56 - 390.48	8.40 - 14.00
Mean Q (MW)	**218.87**	**11.20**
MF range (kg/s)	1600.7 - 4674.8	5.14 - 8.57
Mean MF (kg/s)	**2947.5**	**6.86**
VF range (m³/s)	1541.7 - 4499.2	6.93 - 11.55
Mean VF (m³)	**2835.2**	**9.24**

Table 12: Total heat- and mass-flux, and volumetric flow rate at the LCHF, sorted by advective diffuse and advective focused fluxes.

These results clearly indicate that while heat fluxes can be constrained with the coupled optical-instrumental methods presented in this thesis, inferences on the mass fluxes are highly assumption-dependent, and require additional constraints, such as geochemical data or direct, in situ mass flux measurements. In particular, the crucial factors are (a) the partitioning of heat into high-temperature black smoker and lower-temperature diffuse flow and (b) the origin (nature, characteristics) of this diffuse flow. This partition does not only change among different hydrothermal fields, but also locally within a single hydrothermal field (from area to area). If the diffuse flow is simply ~320°C fluid that has been diluted through mixing with seawater in a shallow, porous subsurface, then its heat flux may be considered as a component of high-temperature flow. Further constraints on the nature of diffuse outflow fluids are required to discriminate if their origin is from mixing of high-temperature end-member hydrothermal fluids and seawater, or from conductive heating, and to more accurately evaluate and estimate water mass and chemical fluxes in the sub-surface from surface observations. Assuming a closed system where all emitted low-temperature (diffuse) fluids results from mixing of high-temperature end-member fluids and ambient seawater,

from which no heat is transferred through conductive cooling in the sub-surface, the fraction of high-temperature end-member fluids (M_f) to emitted fluids (M_{sw}) can be expressed as:

$$M_f/M_{sw} = \frac{C_{sw}(T_0 - T_{sw})}{C_f(T_f - T_0)} \tag{13}$$

where C_{sw} is the specific heat of ambient seawater, T_0 is the measured temperature of diffuse (mixed) hydrothermal fluids, T_{sw} is the temperature of ambient seawater, C_f is the specific heat of high-temperature end-member hydrothermal fluids, and T_f is the maximum measured temperature of high-temperature end-member hydrothermal fluids.

C_{sw} can be calculated as a function of temperature , salinity and pressure of seawater (Nayar et al., 2016, Sharqawy et al., 2010). CTD data (sample GS07-CTD43) collected outside the rift valley on which the LCHF is situated (21 km south of the LCHF) provide salinity data of the LCHF, assuming the salinity and pressure is equal at both localities (Stensland, 2013). For each type of digitized structure a range of fractions ($M_f/M_s w$) are presented (table 13). High-temperature, focused venting is assumed to emit unadulterated end-member hydrothermal fluids ($M_f/M_{sw} = 1$).

	M_f/M_{sw} **range (%)**	**Mean M_f/M_{sw} (%)**
Patches (BM+TW)	$0.50 - 2.02$	1.40
Patches (BM)	1.74 - 5.86	3.05
Cracks (BM)	$7.89 - 11.46$	9.77
Inner mound	31.10 - 33.46	31.92

Table 13: Ranges of calculated mass flux ratios (M_f/M_d) assuming no conductive cooling of hydrothermal fluids.

Constrained total mass fluxes (table 12) and ratios of emitted high-temperature end-member fluids (table 13) are used to calculate the total mass of the corresponding high-temperature end-member fluids (M_{hT}), assuming that all diffuse hydrothermal fluids results from mixing of seawater and high-temperature end-member fluids. Resulting ranges are divided by the calculated density of the emitted (diffuse) fluids [g/cm^3], providing the volumetric flow rate

of high-temperature end-member fluids (V_{hT}). The estimated ranges of mass- and volumetric fluxes of high-temperature end-member fluids are presented in table 14.

	M_{hT} **range**	**Mean** M_{hT}	V_{hT} **range**	**Mean** V_{hT}
Patches (BM+TW)	2.21 - 36.39	21.57	2.12 - 34.92	20.71
Patches (BM)	13.52 - 145.21	46.28	12.97 - 139.83	44.49
Cracks (BM)	4.78 - 9.13	6.99	4.61 - 8.85	6.76
Inner mound	96.62 - 108.84	100.83	96.05 - 108.52	100.35
Black smokers	5.14 - 8.57	6.86	6.93 - 11.55	9.24
Total	122.27 - 308.14	182.53	122.68 - 303.67	181.45

Table 14: Ranges of corresponding mass- and volume fluxes of high-temperature, end-member fluids through diffuse venting. Mass fluxes are given in kg, while volume fluxes are given in dm.

5.3.2 Estimation of chemical fluxes

Besides temperature, another fundamental characteristic of seafloor hydrothermal systems is the chemical composition of the circulating fluids (e.g. Edmond et al., 1979, Von Damm et al., 1985, Campbell et al., 1988), resulting from water-rock reactions at depth. Fluids chemistry has significant impact on the seawater geochemical signature globally (e.g. Elderfield and Schultz, 1996), and locally controls the associated ecosystems, together with physical parameters such as temperature (e.g. Sarrazin et al., 1999, Sarradin et al., 2009). Heat and volume flux estimates, coupled with chemical compositon of hydrothermal fluids, can thus be used to evaluate the range of plausible chemical fluxes both globally (e.g. Elderfield and Schultz, 1996) and at individual sites (e.g. Humphris and Cann, 2000) such as the LCHF. An important complexity however, is the occurrence of subsurface reactions, which may imply a chemical alteration of ascending fluids within the crust, in turn impacting the final composition of hydrothermal fluids sampled at the seafloor. Table 15 presents average compositions for selected major element compositions of end-member, high-temperature fluids. The data is compiled from samples from all four black smokers at the LCHF, from Baumberger et al., 2016 and Pedersen, Rapp, et al., 2010. For the purpose of this discussion and the chemical fluxes presented below, a field-wide average fluid composition derived from these data is used (table 15).

Field-wide chemical flux estimates reported in table 16 are calculated using the fractions of volumetric fluxes presented in table 14, and the average LCHF concentrations for each

element in table 15. Chemistry of hydrothermal fluids is intimately related to the rock type through which the fluids are circulating, and the conditions at which the alteration of host rock occurs. Furthermore, bulk composition of hydrothermal deposits, which precipitate from the high temperature fluids when cooling at the seafloor, can directly be related to the source rock from which the fluids leach. Potentially, these chemical flux estimates at the LCHF, together with assumptions regarding the chemical composition of rocks within the reaction zone at the base of the hydrothermal system, could provide loose constraints on the volume of rocks leached.

	Cl	**Na**	**Si**	**Fe**	**Mn**	**K**	**Sr**
João	497.3	386.7	14.3	21.7	65	34.1	113.8
Camel	521	393.5	14.9	13	68.5	33.7	104.3
Menorah	496	391	15.2	28.5	69.3	35.3	97.2
Sleepy	475	404	15.8	8	73.1	36.8	106
LCHF average	497.3	393.8	15.1	17.8	59.9	52.3	105.3
LCHF seawater	545	453	0	0.2	0.1	9.7	84.8

Table 15: Chemical composition of high-temperature, end-member hydrothermal fluids for selected major elements at the LCHF, and average composition across the entire LCHF. Concentrations in mmol/l. For sites where several sample concentrations are provided, the average of all samples are presented. All chemical concentrations are retrieved from Baumberger et al., 2016 and Pedersen, Rapp, et al., 2010.

Elements	**Minimum flux**	**Maximum flux**	**Mean flux**
Cl($*10^8$mol/yr)	19.187	47.494	38.379
Na($*10^8$mol/yr)	36.260	89.754	53.63
Si($*10^8$mol/yr)	0.583	1.442	0.862
Fe($*10^8$mol/yr)	0.687	1.700	1.016
Mn($*10^8$mol/yr)	2.311	5.721	3.418
K($*10^8$mol/yr)	2.288	5.663	3.384
Sr($*10^8$mol/yr)	4.063	10.056	6.009

Table 16: Average chemical fluxes of high-temperature end-member fractions emitter though advective focused and diffuse venting. The fraction of seawater in diffuse fluids are not included in the calculations. All chemical concentrations used in flux calculations are retrieved from Baumberger et al. (2016) and Pedersen, Rapp, et al. (2010).

5.4 Heat flux extraction at Loki and its implication on the length of the ridge

Constraints placed on the heat-, mass- and chemical fluxes based on in-situ measurements (even when combined with photomosaic imagery) relies heavily on the quality of data, as all results are extrapolated. Based on previous estimates of the heat flux at the LCHF (Stensland, 2013, based on Jean-Baptiste et al., 2004), and results presented in this thesis, the total heat extraction at the LCHF is in the range 146 - 1920 MW, with a probable range of 146-290 MW.

To test the plausibility of the constrained ranges of heat flux through the LCHF, results are compared to the calculated cooling of spreading ridges by Cannat et al. (2004) and Baker (2007)(based on values from Cannat et al., 2004), assuming that all heat extracted along the crust is accreted through the axis. These model can be used to calculate the axis-length needed to continously power a hydrothermal field of this scale. Cannat et al. (2004) estimated the potential heat supply of a ridge spreading at $25\text{mm}^*\text{yr}^{-1}$, assuming an 8km thick layer or peridotite cooling in the lithosphere overlain by a 3km thick layer of pervasively serpentinized peridotite, as 16 MW/km^{-1}. The calculated ranges of Baker (2007) are presented in figure 31, where four scenarios are presented; 3 and 5km of gabbro cooled to 400°C and 700°C. In all four configurations the gabbro is overlaid by 1.4km of basaltic dikes cooled to 400°C. For reference, the spreading rate of the Mohns ridge is estimated as $\sim 15.6 \text{ mm}^*\text{yr}^{-1}$ (Mosar et al., 2002, Vogt, 1986).

If the AMOR has the same configuration as the theoretical ridge in the calculation of Cannat et al. (2004), the axial length of the ridge providing the necessary heat to power the LCHF is approximately 9-24km, with an average of 14km. The range of calculated heat flux of Baker (2007) is $\sim 10\text{MW/km}$ for a spreading rate corresponding to the Mohns ridge. Thus, the axial length needed to power the LCHF, based on this calculation, is 14-39km with an average of 23km. Though the model of Baker (2007) shows spreading rates from 0-150 $\text{mm}^*\text{yr}^{-1}$, the equation on which the model is based accounts for fast-spreading ridges, making the 9-24km more likely. Using the previous results of 720-1920MW (Stensland, 2013) based on plume modelling is not appropriate here, as it would require tapping heat over a ridge length (up to 123 km) longer than the characteristic distance between 2 vent fields on ultra-slow spreading ridges (100 km). On the other hand, the length of ridge necessary to power the heat output constrained in this thesis is consistent with size of convection cells in numerical models for
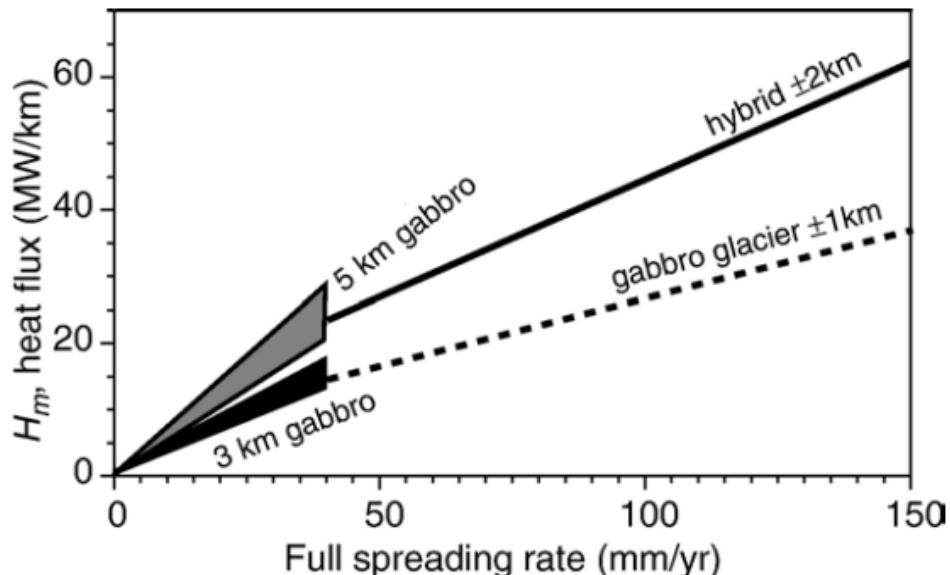
slow ridges (Fontaine et al., 2008).

Figure 31: Calculated hydrothermal cooling of spreading ridges for slow- and fast-spreading ridges. Solid triangles represent the ranges of low- and high-temperature gabbro, cooled to 400°C and 700°C respectively. From Baker, 2007.

6   Conclusions

Generation of photomosaics through seafloor imagery proves a powerful tool for identifying advective hydrothermal outflow at the Loki's Castle Hydrothermal Field. This thesis provides the first detailed constraints on the spatial distribution, characteristics of biomarkers and deposits associated with hydrothermal venting at this site and estimates for heat, mass and chemical fluxes. The total heat flux is constrained to 146-390 MW, with a mean thermal output of 230-290 MW. These tight constraints are clearly distinguishable from previous methods of the heat output through plume measurements, and the method applied here provide better constraints on each parameter and component of hydrothermal flow. The diffusive components accounts for ∼90% of the total heat flux of the site, and from these emitted diffusive fluids the high-temperature end-member fluids account for ∼7% of the total discharged volume. Thus there is a high rate of subsurface mixing between the high-temperature end-member fluids and the cool seawater prior to emission at the seafloor.

7 Future research

Digitization and classification of hydrothermal indicators (e.g. patches, tube worms) provide detailed framework for future research at the LCHF, relevant for multiple scientific fields (e.g. biological, geological and chemical research). Although constraints placed in this thesis are the first of their kind for the LCHF, the estimated heat flux can be further constrained through further integration of temperature measurements. A number of temperature sensors deployed in-situ during the CDeepSea19 research cruise were not recovered in 2020 due to time limitations. Recovery of said sensors at a later time will provide further temperature data points. In addition, measuring the temperature gradient of other vents in the area with the T-gradient board will significantly increase the constraints on the focused outflow. The method can also be applied to similar areas of hydrothermal venting (e.g. Ægir, Fåvne, Jan Mayen vent vields), providing good constraints on the advective hydrothermal heat loss and its contribution in the overall heat budget lost at the ridge axis.

References

Alt, J. C. (1995). Subseafloor processes in mid-ocean ridge hydrothermal systems. *Geophysical monograph - American geophysical union*, *91*, 85–85.

Baker, E. T. (2007). Hydrothermal cooling of midocean ridge axes: Do measured and modeled heat fluxes agree? *Earth and Planetary Science Letters*, *263*(1-2), 140–150.

Baker, E. T., Massoth, G. J., Walker, S. L., & Embley, R. W. (1993). A method for quantitatively estimating diffuse and discrete hydrothermal discharge. *Earth and Planetary Science Letters*, *118*(1-4), 235–249.

Barreyre, T. (2013). *Dynamics and heat fluxes of the lucky strike hydrothermal field (mid-atlantic ridge, 3717'n)* (Doctoral dissertation). Institut de Physique du Globe de Paris Université Paris Diderot. Paris, France.

Barreyre, T., Escartín, J., Sohn, R. A., Cannat, M., Ballu, V., & Crawford, W. C. (2014). Temporal variability and tidal modulation of hydrothermal exit-fluid temperatures at the lucky strike deep-sea vent field, mid-atlantic ridge. *Journal of Geophysical Research: Solid Earth*, *119*, 2543–2566. https://doi.org/10.1002/2013JB010478

Barreyre, T., Escartín, J., Garcia, R., Cannat, M., Mittelstaedt, E., & Prados, R. (2012). Structure, temporal evolution, and heat flux estimates from the lucky strike deep-sea hydrothermal field derived from seafloor image mosaics. *Geochemistry, Geophysics, Geosystems*, *13*(4). https://doi.org/10.1029/2011gc003990

Baumberger, T., Früh-Green, G. L., Thorseth, I. H., Lilley, M. D., Hamelin, C., Bernasconi, S. M., Okland, I. E., & Pedersen, R. B. (2016). Fluid composition of the sediment-influenced loki's castle vent field at the ultra-slow spreading arctic mid-ocean ridge. *Geochimica et Cosmochimica Acta*, *187*, 156–178.

Bischoff, J. L., & Rosenbauer, R. J. (1985). An empirical equation of state for hydrothermal seawater (3.2 percent nacl). *American Journal of Science*, *285*(8), 725–763.

Campbell, A., Palmer, M., Klinkhammer, G., Bowers, T., Edmond, J., Lawrence, J., Casey, J., Thompson, G., Humphris, S., Rona, P., Et al. (1988). Chemistry of hot springs on the mid-atlantic ridge. *Nature*, *335*(6190), 514–519.

Campos, R., & Quintana, J. (2019). *Mosaicing a hydrothermal system on the arctic ridge* (tech. rep.). Coronis Computing SL. Girona, Spain.

Cannat, M. (1993). Emplacement of mantle rocks in the seafloor at mid-ocean ridges. *Journal of Geophysical Research: Solid Earth*, *98*(B3), 4163–4172.

Cannat, M., Cann, J., & Maclennan, J. (2004). Some hard rock constraints on the supply of heat to mid-ocean ridges. *GMS*, *148*, 111–149.

Carazzo, G., Kaminski, E., & Tait, S. (2008). On the rise of turbulent plumes: Quantitative effects of variable entrainment for submarine hydrothermal vents, terrestrial and extra terrestrial explosive volcanism. *Journal of Geophysical Research: Solid Earth*, *113*(B9).

Cooper, M. J., Elderfield, H., & Schultz, A. (2000). Diffuse hydrothermal fluids from lucky strike hydrothermal vent field: Evidence for a shallow conductively heated system. *Journal of Geophysical Research: Solid Earth*, *105*(B8), 19369–19375. https://doi.org/10.1029/2000JB900138

Corliss, J. B., Dymond, J., Gordon, L. I., Edmond, J. M., von Herzen, R. P., Ballard, R. D., Green, K., Williams, D., Bainbridge, A., Crane, K., & van Andel, T. H. (1979). Submarine thermal springs on the galápagos rift. *Science*, *203*(4385), 1073–1083. https://doi.org/10.1126/science.203.4385.1073

Cruise report gs18-218 (Report). (2018). K. G. Jebsen Centre for Deep Sea Research, University of Bergen.

Edmond, J. M., Measures, C., McDuff, R., Chan, L., Collier, R., Grant, B., Gordon, L., & Corliss, J. (1979). Ridge crest hydrothermal activity and the balances of the major and minor elements in the ocean: The galapagos data. *Earth and Planetary Science Letters*, *46*(1), 1–18.

Eickmann, B., Thorseth, I., Peters, M., Strauss, H., Bröcker, M., & Pedersen, R. (2014). Barite in hydrothermal environments as a recorder of subseafloor processes: A multiple-isotope study from the loki's castle vent field. *Geobiology*, *12*(4), 308–321.

Elderfield, H., & Schultz, A. (1996). Mid-ocean ridge hydrothermal fluxes and the chemical composition of the ocean. *Annual Review of Earth and Planetary Science*, *24*, 191–224. https://doi.org/10.1146/annurev.earth.24.1.191

Fontaine, F. J., Cannat, M., & Escartin, J. (2008). Hydrothermal circulation at slow-spreading mid-ocean ridges: The role of along-axis variations in axial lithospheric thickness. *Geology*, *36*(10), 759–762.

Fornari, D. J. (2009). *New miso low-temperature (0°-60°c) self-recording loggers for hydrothermal vent monitoring*. Woods Hole Oceanographic Institution, Multidisciplinary Instrumentation in Support of Oceanography.

Fornari, D., Shank, T., Von Damm, K., Gregg, T., Lilley, M., Levai, G., Bray, A., Haymon, R., Perfit, M., & Lutz, R. (1998). Time-series temperature measurements at high-

temperature hydrothermal vents, east pacific rise 949–51n: Evidence for monitoring a crustal cracking event. *Earth and Planetary Science Letters*, *160*(3), 419–431. https: //doi.org/10.1016/S0012-821X(98)00101-0

German, C., Thurnherr, A., Knoery, J., Charlou, J.-L., Jean-Baptiste, P., & Edmonds, H. (2010). Heat, volume and chemical fluxes from submarine venting: A synthesis of results from the rainbow hydrothermal field, 36 n mar. *Deep Sea Research Part I: Oceanographic Research Papers*, *57*(4), 518–527.

Ginster, U., Mottl, M. J., & Von Herzen, R. P. (1994). Heat flux from black smokers on the endeavour and cleft segments, juan de fuca ridge. *Journal of Geophysical Research: Solid Earth*, *99*(B3), 4937–4950.

Humphris, S. E., & Cann, J. R. (2000). Constraints on the energy and chemical balances of the modern tag and ancient cyprus seafloor sulfide deposits. *Journal of Geophysical Research: Solid Earth*, *105*(B12), 28477–28488.

Jean-Baptiste, P., Bougault, H., Vangriesheim, A., Charlou, J., Radford-Knoery, J., Fouquet, Y., Needham, D., & German, C. (1998). Mantle 3he in hydrothermal vents and plume of the lucky strike site (mar 37 17 n) and associated geothermal heat flux. *Earth and Planetary Science Letters*, *157*(1-2), 69–77.

Jean-Baptiste, P., Fourré, E., Charlou, J.-L., German, C. R., & Radford-Knoery, J. (2004). Helium isotopes at the rainbow hydrothermal site (mid-atlantic ridge, 36 14 n). *Earth and Planetary Science Letters*, *221*(1-4), 325–335.

Jessop, A. M. Et al. (1975). The world heat flow data collection-1975.

Lister, C. (1982). "active" and" passive" hydorthermal systems in the oceanic crust; predicted physical conditions. In *The dynamic seafloors* (pp. 441–470).

Lowell, R. P., Zhang, L., Maqueda, M. A. M., Banyte, D., Tong, V. C. H., Johnston, R. E. R., Harris, R. N., Hobbs, R. W., Peirce, C., Robinson, A. H., & Kolandaivelu, K. (2020). Magma-hydrothermal interactions at the costa rica rift from data collected in 1994 and 2015. *Earth and Planetary Science Letters*, *531*, 115991. https://doi.org/10. 1016/j.epsl.2019.115991

Mittelstaedt, E., Escartín, J., Gracias, N., Olive, J.-A., Barreyre, T., Davaille, A., Cannat, M., & Garcia, R. (2012). Quantifying diffuse and discrete venting at the tour eiffel vent site, lucky strike hydrothermal field. *Geochemistry, Geophysics, Geosystems*, *13*(4), https://agupubs.onlinelibrary.wiley.com/doi/pdf/10.1029/2011GC003991. https : // doi.org/10.1029/2011GC003991

Morton, B., Taylor, G. I., & Turner, J. S. (1956). Turbulent gravitational convection from maintained and instantaneous sources. *Proceedings of the Royal Society of London. Series A. Mathematical and Physical Sciences*, *234*(1196), 1–23.

Mosar, J., Lewis, G., & Torsvik, T. (2002). North atlantic sea-floor spreading rates: Implications for the tertiary development of inversion structures of the norwegian–greenland sea. *Journal of the Geological Society*, *159*(5), 503–515.

Nayar, K. G., Sharqawy, M. H., Banchik, L. D., & Lienhard V, J. H. (2016). Thermophysical properties of seawater: A review and new correlations that include pressure dependence. *Desalination*, *390*, 1–24. https://doi.org/https://doi.org/10.1016/j.desal.2016.02.024

Nielsen, S. G., Rehkämper, M., Teagle, D. A., Butterfield, D. A., Alt, J. C., & Halliday, A. N. (2006). Hydrothermal fluid fluxes calculated from the isotopic mass balance of thallium in the ocean crust. *Earth and Planetary Science Letters*, *251*(1-2), 120–133.

Pedersen, R. B., Rapp, H. T., Thorseth, I. H., Lilley, M. D., Barriga, F. J., Baumberger, T., Flesland, K., Fonseca, R., Fruh-Green, G. L., & Jorgensen, S. L. (2010). Discovery of a black smoker vent field and vent fauna at the arctic mid-ocean ridge. *Nat Commun*, *1*, 126. https://doi.org/10.1038/ncomms1124

Pedersen, R. B., Thorseth, I. H., NygåRd, T. E., Lilley, M. D., & Kelley, D. S. (2010). Hydrothermal activity at the arctic mid-ocean ridges. https://doi.org/10.1029/2008GM000783

Perrone, E. (2009). *Instructions for the operation and maintenance of the ep oceanographic/miso 1010 hi-temperature vent fluid and attitude data logger*. EP Oceanographic, LLC. 5 Spinnaker Lane Pocasset, MA 02559.

Prados, R., Garcia, R., Escartín, J., & Neumann, L. (2011). Challenges of close-range underwater optical mapping, In *Oceans 2011 ieee-spain*, IEEE.

Ramondenc, P., Germanovich, L. N., Von Damm, K. L., & Lowell, R. P. (2006). The first measurements of hydrothermal heat output at 9 50 n, east pacific rise. *Earth and Planetary Science Letters*, *245*(3-4), 487–497.

Rona, P. A., & Trivett, D. A. (1992). Discrete and diffuse heat transfer atashes vent field, axial volcano, juan de fuca ridge. *Earth and Planetary Science Letters*, *109*(1-2), 57–71.

Sarradin, P.-M., Waeles, M., Bernagout, S., Le Gall, C., Sarrazin, J., & Riso, R. (2009). Speciation of dissolved copper within an active hydrothermal edifice on the lucky strike vent field (mar, 37 n). *Science of the total environment*, *407*(2), 869–878.

Sarrazin, J., Juniper, S. K., Massoth, G., & Legendre, P. (1999). Physical and chemical factors influencing species distributions on hydrothermal sulfide edifices of the juan de fuca ridge, northeast pacific. *Marine Ecology Progress Series*, *190*, 89–112.

Sarrazin, J., Rodier, P., Tivey, M. K., Singh, H., Schultz, A., & Sarradin, P.-M. (2009). A dual sensor device to estimate fluid flow velocity at diffuse hydrothermal vents. *Deep Sea Research Part I: Oceanographic Research Papers*, *56*(11), 2065–2074.

Schultz, A., Delaney, J., & McDuff, R. (1992). On the partitioning of heat flux between diffuse and point source seafloor venting. *Journal of Geophysical Research: Solid Earth*, *97*(B9), 12299–12314.

Seewald, J. S., Doherty, K. W., Hammar, T. R., & Liberatore, S. P. (2002). A new gas-tight isobaric sampler for hydrothermal fluids. *Deep Sea Research Part I: Oceanographic Research Papers*, *49*(1), 189–196. https://doi.org/https://doi.org/10.1016/S0967-0637(01)00046-2

Sharqawy, M. H., Lienhard, J. H., & Zubair, S. M. (2010). Thermophysical properties of seawater: A review of existing correlations and data. *Desalination and water Treatment*, *16*(1-3), 354–380.

Speer, K. G., & Rona, P. A. (1989). A model of an atlantic and pacific hydrothermal plume. *Journal of Geophysical Research: Oceans*, *94*(C5), 6213–6220.

Stein, C. A., & Stein, S. (1994). Constraints on hydrothermal heat flux through the oceanic lithosphere from the global heat flow. *J. Geophys. Res.*, *99*, 3081–3095.

Stein, J. S., & Fisher, A. T. (2001). Multiple scales of hydrothermal circulation in middle valley, northern juan de fuca ridge: Physical constraints and geologic models. *Journal of Geophysical Research: Solid Earth*, *106*(B5), 8563–8580.

Stensland, A. (2013). *Dissolved gases in hydrothermal plumes from arctic vent fields* (Master's thesis). University of Bergen. Bergen, Norway.

Van Dover, C. (2000). *The ecology of deep-sea hydrothermal vents*. Princeton University Press.

Veirs, S. R., McDuff, R. E., & Stahr, F. R. (2006). Magnitude and variance of near-bottom horizontal heat flux at the main endeavour hydrothermal vent field. *Geochemistry, Geophysics, Geosystems*, *7*(2).

Viflot, T., Reeves, E. P., Vulcano, F., Seewald, E., Roerdink, D., Steen, I. H., & Barreyre, T. (2019). Conductive cooling and microbial carbon transformations in diffuse hydrothermal fluids at loki's castle. *Goldschimdt Abstracts*, *2019*, 3510.

Vogt, P. (1986). Geophysical and geochemical signatures and plate tectonics, In *The nordic seas*. Springer.

Von Damm, K., Edmond, J., Grant, B., Measures, C., Walden, B., & Weiss, R. (1985). Chemistry of submarine hydrothermal solutions at 21 n, east pacific rise. *Geochimica et Cosmochimica Acta*, *49*(11), 2197–2220.

Wilcock, W. S., & Delaney, J. R. (1996). Mid-ocean ridge sulfide deposits: Evidence for heat extraction from magma chambers or cracking fronts? *Earth and Planetary Science Letters*, *145*(1-4), 49–64.